STRUCTURAL SCIENCE CRYSTAL ENGINEERING MATERIALS

ISSN 2052-5206

Hexagonal RMnO$_3$: a model system for two-dimensional triangular lattice antiferromagnets

Hasung Sim, Joosung Oh, Jaehong Jeong, Manh Duc Le and Je-Geun Park*

Center for Correlated Electron Systems, Institute for Basic Science (IBS) and Department of Physics and Astronomy, Seoul National University, Seoul 08826, Korea. *Correspondence e-mail: jgpark10@snu.ac.kr

Received 2 October 2015
Accepted 19 November 2015

Edited by A. J. Blake, University of Nottingham, England

Keywords: multiferroic materials; ferroelectricity; magnetic structures; magnetic frustration; spin-lattice coupling.

The hexagonal RMnO$_3$(h-RMnO$_3$) are multiferroic materials, which exhibit the coexistence of a magnetic order and ferroelectricity. Their distinction is in their geometry that both results in an unusual mechanism to break inversion symmetry and also produces a two-dimensional triangular lattice of Mn spins, which is subject to geometrical magnetic frustration due to the antiferromagnetic interactions between nearest-neighbor Mn ions. This unique combination makes the h-RMnO$_3$ a model system to test ideas of spin-lattice coupling, particularly when both the improper ferroelectricity and the Mn trimerization that appears to determine the symmetry of the magnetic structure arise from the same structure distortion. In this review we demonstrate how the use of both neutron and X-ray diffraction and inelastic neutron scattering techniques have been essential to paint this comprehensive and coherent picture of h-RMnO$_3$.

1. Introduction

The magnetic and crystal structures of multiferroic materials play a crucial role in determining their physical and functional properties. In the case of some of the perovskite manganites, it was established that ferroelectric order follows as a result of a spiral magnetic structure and the inverse Dzyaloshinskii–Moriya interaction (Kimura *et al.*, 2003). In others, a zigzag magnetic order gives rise to ionic displacements *via* exchange-striction (Mochizuki *et al.*, 2011). Similar mechanisms may lie at the root of the magnetoelectric coupling in the hexagonal manganite family, which is the focus of this article. Whilst RMnO$_3$ compounds with lighter rare-earth elements (R = La–Ho) can be stabilized with an orthorhombic distorted perovskite structure, the smaller ionic radii of elements at the end of the lanthanide series result in a close-packed hexagonal structure with the space group $P6_3/mmc$ at high temperatures.

Unlike the perovskite manganites, where magnetic and ferroelectric ordering temperatures coincide, the hexagonal manganites are type-I multiferroics with quite different transition temperatures: ferroelectric T_C (> 1000 K) and magnetic T_N (< 100 K). This is because inversion symmetry is broken in these materials by the cooperative rotation of MnO$_5$ bipyramids (Van Aken *et al.*, 2004) rather than due to a noncentrosymmetric magnetic structure. Nonetheless, strong magnetoelastic coupling effects have been observed in the hexagonal manganites, notably a large displacement of Mn ions further towards or away from their apical oxygen ion at the Néel temperature (Lee *et al.*, 2008). The initial Mn off-centering, however, occurs at the ferroelectric Curie point, and appears to correlate with the rare-earth ionic size. In addition to being exaggerated by the magnetic ordering, the nature of the initial Mn off-centering (whether towards or

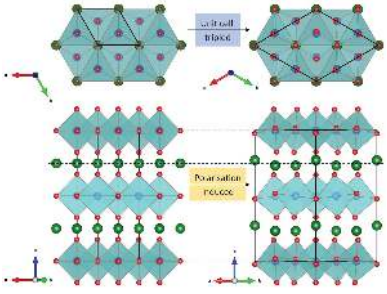

away from the apical oxygen) appears to determine the symmetry of the magnetic structure (Fabrèges *et al.*, 2009).

There is thus a strong link between the magnetic and crystal structures, and this carries over into the crystal and magnetic dynamics. For example, it has been recognized that there is a large degree of coupling between the magnons and phonons in the hexagonal manganites (Oh *et al.*, 2016), although no electromagnons have yet been reported. Finally, the magnon spectrum has also yielded evidence of magnon decay and nonlinear magnon–magnon interactions in a relatively large spin ($S = 2$) system, due to the noncollinear magnetic structure arising from the geometrically frustrated triangular lattice of Mn^{3+} ions (Oh *et al.*, 2013). In this article we will review and explore both aspects of the magneto-electric coupling, with the structural aspects discussed in §2 and the dynamical properties in §3.

A short note of disclaimer: Although we tried to be comprehensive in covering the physics of *h*-RMnO$_3$, inevitably we could not include all the interesting topics of *h*-RMnO$_3$ in our article. Mainly because of the lack of space, here we focused on the spin-lattice issue in a bulk form, leaving out some other interesting works and different properties in a nanocrystalline (Bergum *et al.*, 2011) or film form, yet less related to our main point.

2. Structure

The rare-earth manganite compounds RMnO$_3$ adopt one of two polymorphs: a distorted perovskite structure which is stabilized for larger R^{3+} cations; and a hexagonal polymorph which is a stable phase for smaller R^{3+}. For intermediate-sized cations, either structures may be stabilized by growth in an oxygen-excess or -deficient atmosphere (Harikrishnan *et al.*, 2009) or with the application of pressure (Zhou *et al.*, 2006). Whilst they exhibit both ferroelectricity and antiferromagnetism, the magnetoelectric coupling between them seems likely to occur *via* distortions of the crystal structure. The ferroelectric Curie temperature is around $\gtrsim 1000$ K and has a slight dependence on the cation size, with YMnO$_3$ having the lowest T_C and the largest ionic radius. The Néel temperature is some ten times lower, $T_N \lesssim 100$ K, which may be due to the geometrical magnetic frustration of the triangular lattice of Mn spins. We note that the superexchange interactions between nearest-neighbour Mn–Mn pairs is quite strong, giving a Curie–Weiss temperature (which is proportional to the sum of the exchange interactions) of ~ 600 K. The transition temperatures and the crystal and magnetic space-group symmetry is summarized in Fig. 1, in the order of increasing R^{3+} cation size. As we noted above, the actual magnetic ordering is pushed towards a much lower temperature probably because of the intrinsic geometrical frustration of the triangular lattice and also the low dimensionality. Therefore, we do not think that the big difference between the FE and AFM transition temperatures itself indicates a weaker magnetoelectric coupling for *h*-RMnO$_3$, although this argument has been used in some corner of the community.

Whilst some studies have reported only a single phase transition above room temperature, others have found two, which have led to divergent views on the nature of the ferroelectric transition and the origin of ferroelectricity in the hexagonal manganites. There are two principle structure distortions that lower the symmetry of the system from non-polar (paraelectric) $P6_3/mmc$ to polar (ferroelectric) $P6_3cm$. Whilst the Γ_2^- mode produces a net polarization, the unit cell tripling K_3 mode does not. Calculations show, however, that the K_3 mode is the primary order parameter that induces the Γ_2^- distortion due to geometric factors (Van Aken *et al.*, 2004), making the hexagonal manganites improper ferroelectrics. As the K_3 mode also results in the trimerization of the Mn sublattice, it affects, and is affected by, magnetic ordering and so provides a microscopic mechanism for the magneto-electric coupling. If, on the other hand, the two distortions are independent as may be the case if two distinct transitions exist at which each distortion is stabilized, then this mechanism is invalid.

We thus begin this section with a discussion of the high temperature transitions, and the nature of the ferroelectricity, before moving on to a discussion of the magnetic structure and its connection to the crystal structure and trimerization distortion.

2.1. The ferroelectric transition

Fig. 2 shows the crystal structures of the non-polar (paraelectric) $P6_3/mmc$ and polar (ferroelectric) $P6_3cm$ phases. The four space groups that are both subgroups of $P6_3/mmc$ and supergroups of $P6_3cm$ are each associated with a symmetry

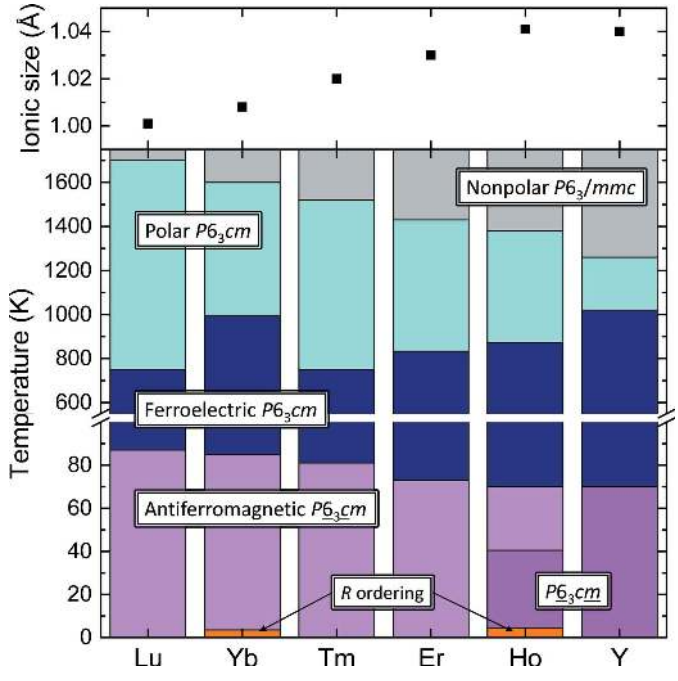

Figure 1
Summary of phase diagrams of several hexagonal RMnO$_3$. Transition temperatures are taken after Chae *et al.* (2012), Lonkai *et al.* (2004), Abrahams (2001), Gibbs *et al.* (2011), Fan *et al.* (2014) and Lorenz (2013).

lowering mode (Lonkai *et al.*, 2004), and their relationship is also shown in Fig. 2. The Γ_1^+ breathing mode affects only the z position of the apical oxygen and does not change the space-group symmetry. The two K modes result in a $\sqrt{3} \times \sqrt{3}$ tripling of the unit cell, either by tilting of the MnO_5 trigonal bipyramid (K_3) or its displacement along a (K_1). This results in extra peaks in the diffraction pattern that are clearly visible in the experimental data. However, these modes do not produce a net ferroelectric polarization; although the K_3 mode produces a local dipole moment, this is cancelled globally. Rather, the ferroelectricity only arises from the Γ_2^- distortion, which allows the displacements of the R and Mn cations and oxygen anions with respect to each other along the c axis. However, this distortion by itself does not result in a unit cell tripling and can yield a proper ferroelectric phase with $P6_3mc$ symmetry.

Early dielectric constants (Coeuré *et al.*, 1966) and pyroelectric current (Ismailzade & Kizhaev, 1965*a*,*b*) measurements suggested that the ferroelectric transition should be below 1000 K, which is correlated with a change in the slope of the resistivity (Choi *et al.*, 2010). However, neutron (Lonkai *et al.*, 2004; Gibbs *et al.*, 2011) and X-ray (Lonkai *et al.*, 2004; Nénert *et al.*, 2007) diffraction studies indicated a unit cell tripling at higher temperatures $\sim$ 1250 K. These observations

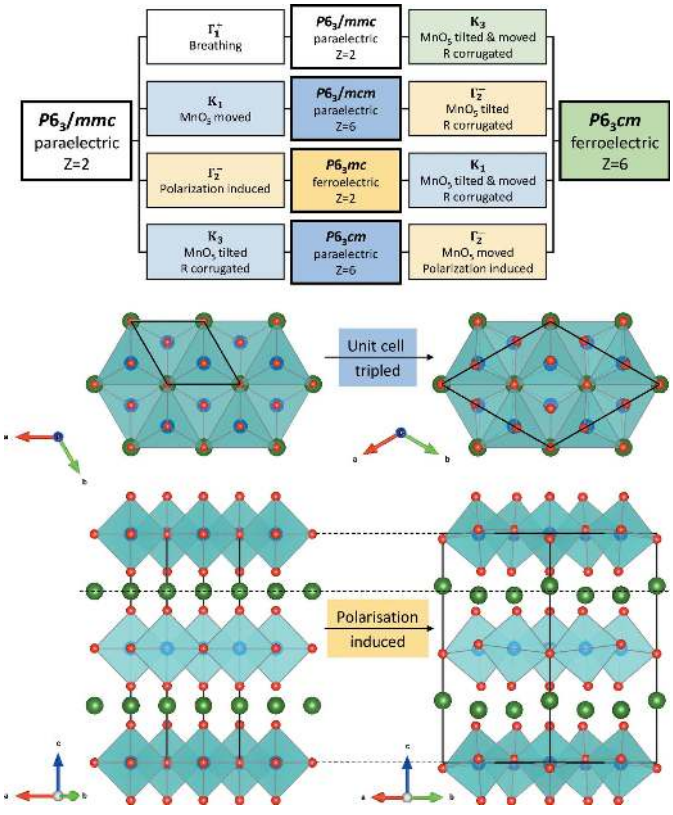

Figure 2
Analysis of symmetry and structural changes at high temperature. Four possible routes from $P6_3/mmc$ to $P6_3cm$ that are related to the ferroelectric and structural transitions. The symmetry analyses are adopted from Lonkai *et al.* (2004), Nénert *et al.* (2005) and Fennie & Rabe (2005).

can only be reconciled if the higher temperature transition arises either from the K_1 or K_3 mode, whilst the Γ_2^- mode is stabilized below the lower temperature transition. This would yield either a paraelectric $P6_3/mcm$ or antiferroelectric $P6_3cm$ intermediate phase. The former case was favoured by Nénert *et al.* (2005), whilst Lonkai *et al.* (2004) and Gibbs *et al.* (2011) showed from detailed analysis of their neutron diffraction patterns that the MnO_5 bipyramid is indeed tilted rather than simply displaced, establishing that the K_3 mode is stabilized and the intermediate structure is $P6_3cm$.

This scenario is further supported by *ab initio* calculations, which showed that the K_3 mode is strongly unstable in the symmetric $P6_3/mmc$ structure (Fennie & Rabe, 2005), whereas the K_1 mode is stable with high calculated phonon frequencies. A decomposition of the atomic displacements between the $P6_3/mmc$ structure and the room temperature $P6_3cm$ structure in terms of the normal modes also shows that the amplitude of the K_3 mode (0.93 Å) is much greater than K_1 (0.03 Å) or Γ_2^- modes (0.16 Å).

Considering all the experimental and theoretical studies together, it is of our view that the first high-temperature transition above 1200 K is from $P6_3/mcm$ to $P6_3cm$, while the second transition at around 900–1000 K is the isostructural transition involving a huge increase of electric polarization and so the intermediate phase is the polar $P6_3cm$ space group. Because of this polar nature of the intermediate phase, it is most likely that *h*-RMnO$_3$ already has nonzero electric polarization below the first high-temperature phase transition, although it seems to have a smaller value. Only when it undergoes the second isostructural transition below 1000 K does it begin to develop the large polarization value of around 5 μC cm^{-2} at room temperature.

2.1.1. Origin of ferroelectricity. The first principles calculations point to a mechanism underlying the ferroelectricity in the *h*-RMnO$_3$ system. Van Aken & Palstra (2004) were the first to suggest the principles of what was later termed 'geometric ferroelectricity', in which in certain geometries global inversion symmetry may be broken by a polyhedral tilt. For *h*-RMnO$_3$, the triangular symmetry of the Mn—O plane means that the K_3 tilt of the MnO_5 bipyramid satisfies this condition, which is not the case for the octahedral tilts of the perovskite structure. The next essential ingredient is the coupling of this distortion to the polar mode Γ_2^-, which Fennie & Rabe (2005) showed to have a nonzero equilibrium displacement when the amplitude of the K_3 mode is finite. Thus, the K_3 mode acts as a 'geometric field' that pushes the equatorial oxygen ions away from the Mn plane, giving unequal R—O_{eq} distances due to the buckling of the R-layer, which accompanies the MnO_5 tilt.

Although this coupling is initially nonlinear and small, it only becomes linear and significant above a cross-over threshold. This cross-over temperature is calculated to be $\sim$ 100 K (Fennie & Rabe, 2005), which is about the same order as the difference between the upper and lower transition temperatures seen in the diffraction and physical properties measurements as discussed above. Thus, the two transitions may be explained, in part, by the nature of the ferroelectricity

in *h*-RMnO$_3$; although a finite polarization exists below the initial structure transition between $P6_3/mmc$ and $P6_3cm$, it only becomes significant after 'turning on' the polar mode of Γ_2^- at a lower temperature. This scenario may be supported by our high-resolution X-ray diffraction measurements at high temperatures, shown in Fig. 3. Peaks from the tripled unit cell, outlined in red in Fig. 3, appear below ~ 1250 K, which correlates well with a sharp increase in the c lattice constant, shown in Fig. 4. The temperature dependence of the integrated intensity of 102 Bragg peaks, drawn in Fig. 4, is best fit by a model with two transitions at 1225 (9) and 1012 (32) K, if the critical exponent is restricted to be $\beta = \frac{1}{2}$ required for a second-order Landau phase transition. The ratio of the magnitude of the upper to lower transitions, 4.66, is also close to the amplitude ratio of the K_3 and Γ_2^- modes, 5.8 as found in the theoretical studies (Fennie & Rabe, 2005), suggesting that the upper transition may be due to the K_3 mode and the lower transition to the Γ_2^- mode.

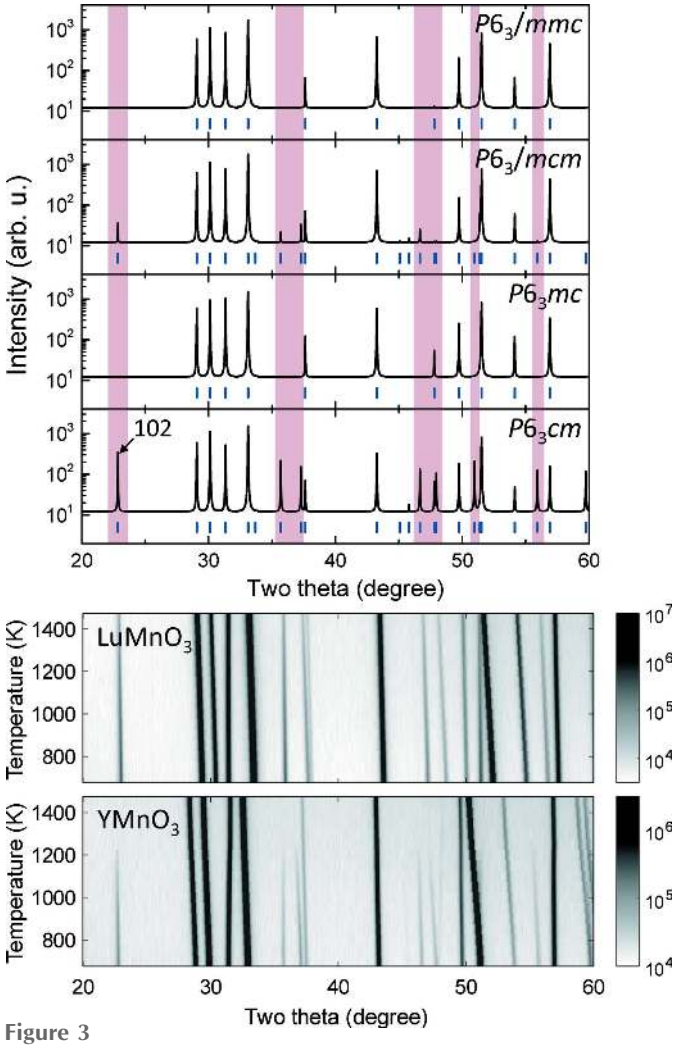

Figure 3
(Top) Simulated diffraction patterns for four possible space groups as shown in Fig. 2. A region of interest in the diffraction patterns is marked by shading. (bottom) Temperature dependence of our high-resolution X-ray diffraction patterns for LuMnO$_3$ and YMnO$_3$ taken at high temperature.

As another indicator for the source of the ferroelectricity, the Born effective charges estimated from the first principles calculations by Van Aken & Palstra (2004) were found to be quite close to the nominal valences, indicating that the ferroelectricity should not result from strong hybridization effects. However, Cho *et al.* (2007) observed several peaks in the oxygen K-edge X-ray absorption spectrum, which may only be explained by a strong overlap between the empty *d*-states of rare-earth elements and the O *p*-states. Further, the measurements also showed striking differences depending on whether the incident light was polarized parallel or perpendicular to the *c* axis, indicating that this hybridization is highly anisotropic and stronger along the *c* axis. This is consistent with later optical conductivity measurements by Zaghrioui *et al.* (2008), who determined that the Born effective charge tensor is anisotropic with $Z^*_{zz}(\mathrm{O}) \simeq -3$ and $Z^*_{zz}(R, \mathrm{Mn}) \simeq 4.5$, relatively enhanced compared with the ionic expectations. Similarly a separate X-ray diffraction study using the maximum entropy method (MEM) by Kim *et al.* (2009) showed an increased hybridization effect between R ions at the 2*a* Wyckoff sites and the equilateral O ions below the

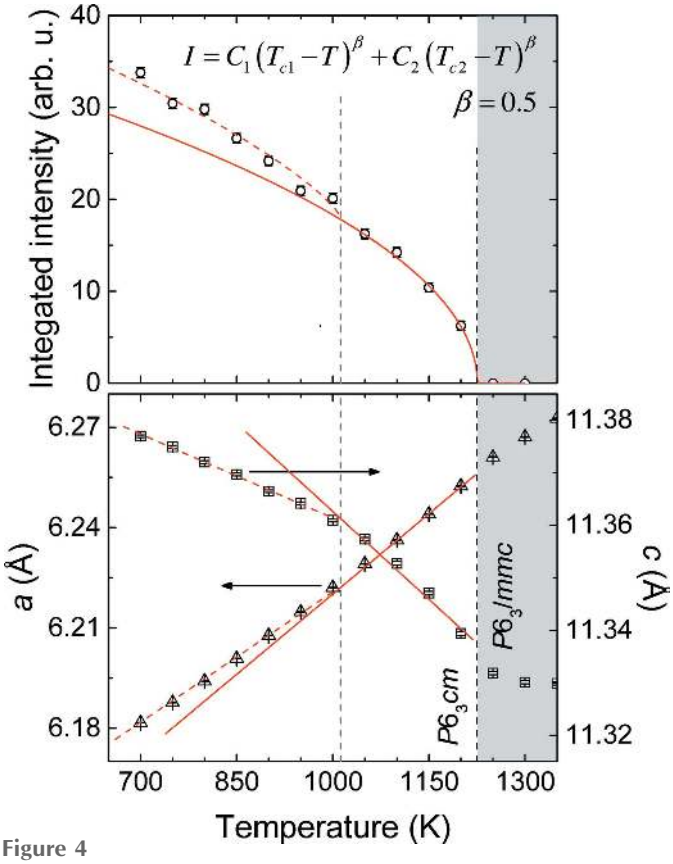

Figure 4
(Top) Temperature dependence of the integrated intensity of the 102 Bragg peak and the lattice parameters in YMnO$_3$. The lines represent our theoretical calculations using Landau–Ginzburg analysis with one order parameter (solid) and two order parameters (dashed line). The structural transition ($P6_3/mmc$ to $P6_3cm$) and the secondary transition are clearly visible at 1225 and 1012 K, respectively. (bottom) The temperature dependence is presented of the two lattice constants with the lines serving as guides for the eye at both below and above the second transition at 1012 K.

second transition in the ferroelectric phase. These observations also suggest that hybridization in a traditional d^0 picture should have some role in generating the large observed polarization, above and beyond that produced from purely geometric displacements. A more recent work by Tyson *et al.* (2011), based on the accurate determination of the atomic positions derived from both diffraction and X-ray absorption fine spectra, concurs with the previous experimental works in finding a strongly anisotropic Born effective charge tensor and strong hybridization effects.

2.2. Magnetic transition

Hexagonal $R\mathrm{MnO_3}$ compounds exhibit an antiferromagnetic transition near $T_\mathrm{N} \simeq 100$ K due to the superexchange interactions between $\mathrm{Mn^{3+}}$ moments. In addition, those with magnetic rare-earth ions (R = Ho, Er, and Tm) also show an additional magnetic transition below 10 K, arising from the ordering of the rare-earth moments on the 2*a* Wyckoff sites. The rare-earth moments on the other (4*b*) sites order concurrently with the Mn triangular lattice at T_N, due to an Mn–R superexchange interaction. The rare-earth moments are thought to align along the *c* axis and are ordered antiferromagnetically within the *ab* plane (Alonso *et al.*, 2000; Curnoe & Munawar, 2006), although a neutron diffraction study suggested that the rare-earth moments at the 2*a* site may lie in the *ab* plane (Fabrèges *et al.*, 2008). In this review, we will focus primarily on the Mn moment ordering.

2.2.1. Magnetic point groups. No structural change has been observed at T_N, so the crystallographic space group remains the same as the $P6_3cm$ space group, from which the magnetic space group can be determined. The magnetic structure was found to have a propagation vector $\mathbf{k} = (0, 0, 0)$, which gives rise to four possible one-dimensional representations, namely Γ_1 (A_1), Γ_2 (A_2), Γ_3 (B_1), Γ_4 (B_2), and two two-dimensional representations, Γ_5 (A) and Γ_6 (B), which are illustrated in Fig. 5. Rather than the Γ symbols, the international (Hermann–Mauguin) notation, where symmetry operators that retain time reversal symmetries are primed or underlined, is also often used in the literature, with the following equivalence: $P6_3cm$ (Γ_1), $P6_3\underline{c}m$ (Γ_2), $P\underline{6}_3c\underline{m}$ (Γ_3), $P\underline{6}_3\underline{c}m$ (Γ_4), $P6_3$ (Γ_5) and $P\underline{6}_3$ (Γ_6) (Lorenz, 2013; Fiebig *et al.*, 2003). The spin arrangements corresponding to these representations are illustrated in Fig. 5.

The magnetic structures represented in Fig. 5 that preserve the sixfold rotational symmetry are essentially the 120° structure predicted for a classical Heisenberg antiferromagnet on the triangular lattice, which are either antiferromagnetically ($\Gamma_{1,2,5}$) or ferromagnetically ($\Gamma_{3,4,6}$) coupled along the *c* axis. For the Γ_2 and Γ_3 representations, the moments can have components along the *c* axis, which are (anti-)ferromagnetically coupled along the *c* axis for the (Γ_3) Γ_2 structures. For comparison, the moments are restricted to the hexagonal plane for the Γ_1 and Γ_4 structures. In the case of the one-dimensional representations, the in-plane moments are constrained to be perpendicular ($\Gamma_{1,4}$) or parallel ($\Gamma_{2,3}$) to the *a* axis, whilst for the two-dimensional representations they may take a constant angle φ with respect to the crystallographic axis. The two-dimensional representations may also have moment components along the *c* axis. Finally, Γ_1 and Γ_3 are homometric (Brown & Chatterji, 2006) so cannot be distinguished by powder neutron diffraction, as are Γ_2 and Γ_4.

2.2.2. Determination of magnetic structure. Two main experimental techniques have been used to determine the magnetic structures of *h*-$R\mathrm{MnO_3}$: neutron diffraction and second harmonic generation (SHG), although magnetometry may also be used to infer the presence of a Γ_2 order if a weak ferromagnetic signal is measured, which is not the case for the *h*-$R\mathrm{MnO_3}$ compounds. Whilst neutron powder diffraction is a common and powerful tool to determine a magnetic structure, it cannot distinguish between the Γ_1 and Γ_3 structures, or between the Γ_2 and Γ_4 structures. This may be resolved by single-crystal polarized neutron diffraction experiments, but the measurements are challenging and have only been reported for $\mathrm{HoMnO_3}$ and $\mathrm{YMnO_3}$ (Brown & Chatterji, 2006). On the other hand, SHG can, in principle, distinguish between all the possible structures (Fiebig *et al.*, 2000). For light incident along the *c* axis, no second harmonic signal implies either one of the Γ_1 or Γ_2 structures, whilst a signal polarized parallel to the *a* axis indicates the Γ_4 structure and that polarized perpendicular to the *a* and *c* axes indicates the Γ_3 structure (Fiebig *et al.*, 2003). Although the Γ_1 and Γ_2 structures can be distinguished using light polarized parallel to the *c* axis, in this case a second harmonic signal from the ferroelectric polarization also exists (Fiebig *et al.*, 2005). Alternatively, the behaviour of the second harmonic signals across a metamag-

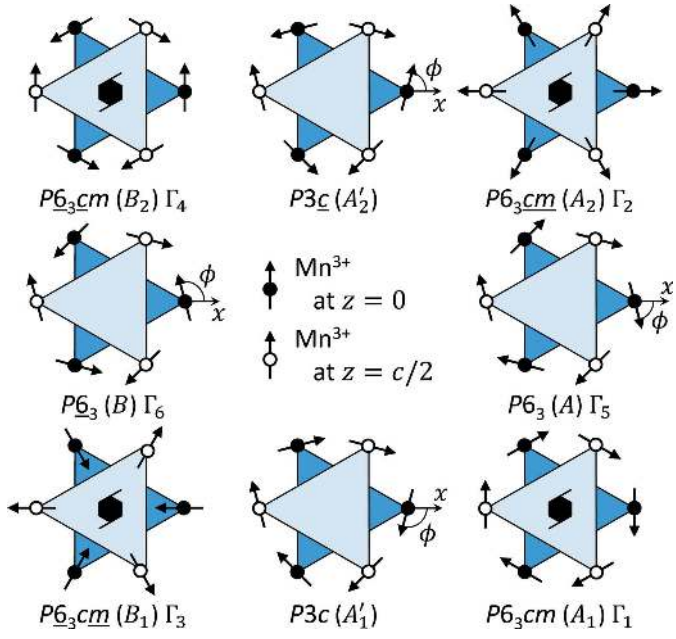

Figure 5
Magnetic structures based on the space group $P6_3cm$ (No. 185). Four possible magnetic point groups in one-dimensional basis vectors and four intermediate ones are shown at the corner and between them, respectively (reprinted from Fiebig *et al.*, 2003, with permission from American Institute of Physics).

netic transition under applied magnetic field can serve to elucidate the zero-field magnetic structure (Fiebig *et al.*, 2003).

2.2.3. Spin reorientation. For most *h*-*R*MnO_3 compounds, the SHG and neutron data are consistent, yielding a Γ_4 structure for R = Yb, Tm and Er in zero field. In the case of $YMnO_3$, powder neutron diffraction determined the structure to have either Γ_1 or Γ_3 symmetry (Muñoz *et al.*, 2000; Lee *et al.*, 2005, 2008; Sekhar *et al.*, 2005), whilst the SHG work showed a Γ_3 structure (Fiebig *et al.*, 2003; Degenhardt *et al.*, 2001). However, a detailed polarized neutron diffraction study (Brown & Chatterji, 2006) concluded that it is actually the Γ_6 structure (*i.e.* between Γ_3 and Γ_4) but with an angle of $\phi = 11^\circ$, which is closer to the Γ_3 structure.

$LuMnO_3$ is another case where the SHG and neutron diffraction disagree, in that SHG found domains with a Γ_4 structure at high temperatures, but Γ_3 at low temperatures with an intermediate Γ_6 phase coexisting with either of the others (Fiebig *et al.*, 2000). However, neutron diffraction measurements saw no evidence of the Γ_3 structure at any temperature (Park *et al.*, 2010; Tong *et al.*, 2012): some Bragg peaks such as 100 expected for the Γ_3 structure are absent in the experimental data. Furthermore, no evidence of the second phase transition was found in the measurements of physical properties such as dielectric constants (Katsufuji *et al.*, 2001). However, Toth *et al.* (2012) reported observing additional peaks in the neutron powder diffraction pattern at low temperatures, and suggest that this arises from an unidentified incommensurate magnetic phase. Whilst this needs to be confirmed independently, it is conceivable that this may explain the SHG measurements.

The case of $HoMnO_3$ is clearer, however, and a spin reorientation transition from Γ_4 to Γ_3 structures with decreasing temperatures is seen both in SHG (Fiebig *et al.*, 2003) and neutron (Vajk *et al.*, 2005; Chatterji *et al.*, 2014) measurements, as reproduced in Figs. 6(*a*) and (*b*), respectively. The transition temperature $T_{SR} = 33$ K is also visible in the physical properties, such as the dielectric constant and magnetic susceptibility (dela Cruz *et al.*, 2005), heat capacity (Lorenz *et al.*, 2005) and electric polarization (Hur *et al.*, 2009), as shown in Fig. 7(*a*). The mechanism behind this transition is argued to be due to a change in the sign of the structural trimerization distortion (Fabrèges *et al.*, 2009), and a spin-lattice coupling *via* the single-ion anisotropy, which is discussed in detail in §2.3.

For other *h*-*R*MnO_3 compounds, although there have been some reports of anomalies in between T_N and the rare-earth ordering temperature of $\lesssim 10$ K in their physical properties (Iwata & Kohn, 1998; Fan *et al.*, 2014), these observations have not been confirmed by other studies in many cases (Sugie *et al.*, 2002; Katsufuji *et al.*, 2002; Sekhar *et al.*, 2005). Furthermore, no change was observed in the neutron diffraction patterns (Park *et al.*, 2002; Sekhar *et al.*, 2005; Fabrèges *et al.*, 2008, 2009) or second harmonic generation spectra (Fiebig *et al.*, 2003).

Finally, in all *h*-*R*MnO_3 a metamagnetic transition occurs under an applied magnetic field from the zero-field Γ_3 or Γ_4 structure to the Γ_2 structure, as shown in Fig. 6(*a*), and this transition may be hysteretic (Fennie & Rabe, 2005). The phase transitions under an applied field have been confirmed by some physical property measurements (Sugie *et al.*, 2002; Yen *et al.*, 2007), although Yen *et al.* (2007) found no hysteresis in their data. This latter observation was attributed to the weak ferromagnetic moment induced by spin canting that is permitted in the Γ_2 phase (Sugie *et al.*, 2002). The combination of this rare-earth moment together with the sensitivity of the Mn spin direction to the lattice and the Mn–*R* coupling leads to a very rich magnetic phase diagram for $HoMnO_3$ with intriguing critical behaviour at low temperatures (Choi *et al.*, 2013).

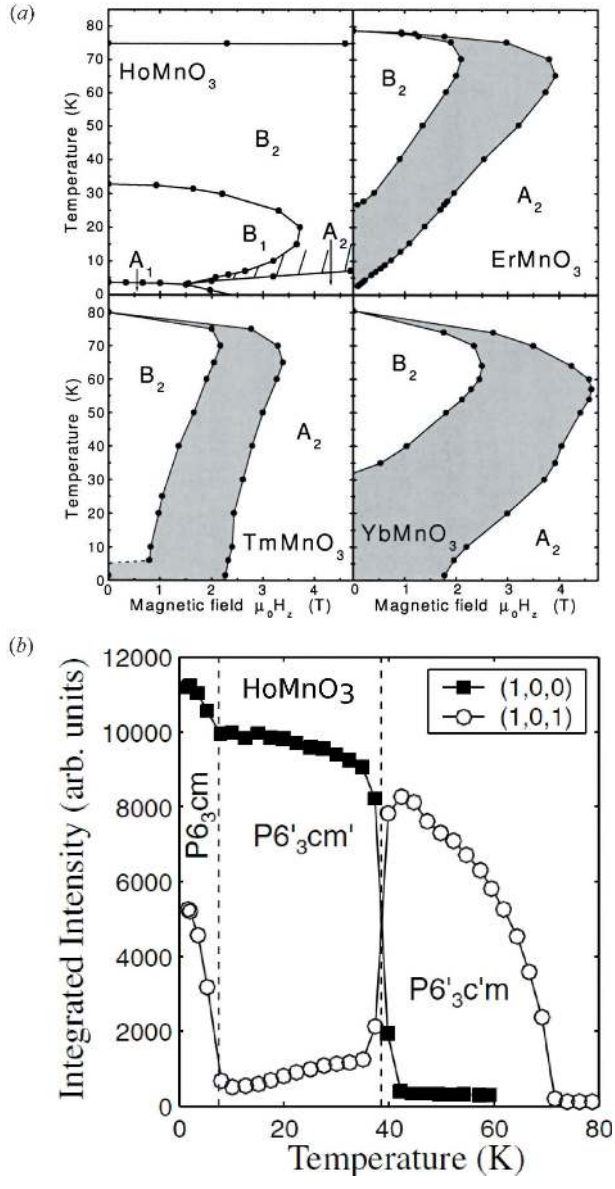

Figure 6
(*a*) Phase diagram of several *R*MnO_3 compounds using second harmonic generation (SHG) results. (*b*) Peak intensity of $HoMnO_3$ using powder neutron diffraction data. Both show changes due to the spin reorientation at lower temperatures. Reprinted from Fiebig *et al.* (2003), with permission from American Institute of Physics, and Vajk *et al.* (2005). Copyright © 2005. American Physical Society.

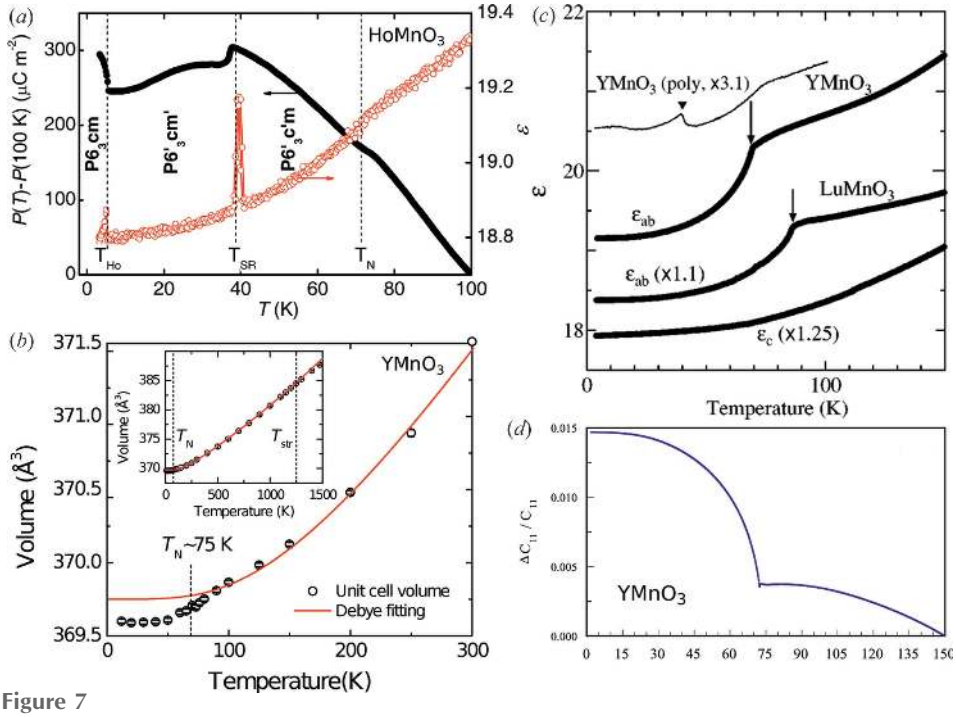

Figure 7
Several physical properties show distinctive changes at the spin reorientation transition temperature. Temperature dependence is shown of (*a*) polarization, (*b*) unit-cell volume, (*c*) dielectric constant and (*d*) elastic moduli. Reprinted with permission from Hur *et al.* (2009) (Copyright © 2009, American Physical Society), Park *et al.* (2010) (Copyright © 2010, American Physical Society), Katsufuji *et al.* (2001) (Copyright © 2001, American Physical Society) and Poirier *et al.* (2007) (Copyright © 2007, American Physical Society).

2.3. Spin-lattice coupling

The strong nearest-neighbour superexchange interaction between the Mn spins favours a structure where the direction of the moments rotates by 120° between neighbours. However, this leaves the spin free to adopt an overall rotation angle φ with respect to the crystallographic axes. For example, first principles calculations by Solovyev *et al.* (2012) suggested that this direction is set by the single-ion anisotropy, which in turn is determined by the K_1 structure distortion that shifts the Mn ions along the direction of one of the three Mn—O_{eq} bonds. This *trimerization* distortion is illustrated in Fig. 8. If the Mn ion is shifted towards the equilateral oxygen (the Mn x coordinate is less than $\frac{1}{3}$, giving small trimers, in Fig. 8*b*), then the moments tend to align in this direction and the magnetic structure is either the Γ_1 or Γ_4 structures. On the other hand, if they are shifted away ($x>\frac{1}{3}$, Fig. 8*c*), then the moments prefer to be perpendicular to the bond, giving either the Γ_2 or Γ_3 structure (Solovyev *et al.*, 2012). The interlayer exchange interactions then determine which of these possible states are adopted. Interestingly, Solovyev *et al.* (2012) found that for both $YMnO_3$ ($x>\frac{1}{3}$) and $LuMnO_3$ ($x<\frac{1}{3}$), the interlayer interactions are antiferromagnetic, but that in both cases the second neighbour interplanar interaction between overlapping triangles J_2^c always has a smaller magnitude than that between neighbouring triangles $J_2^{c\prime}$ (as denoted in Fig. 8), which thus favours the Γ_3 ($YMnO_3$) or Γ_4 ($LuMnO_3$) structures as the J_2^c pairs favour a ferromagnetic alignment.

However, the difference in total energy for these structures (Γ_3 or Γ_4) due to the single-ion anisotropy is quite small so alternative calculations by Das *et al.* (2014) give the Γ_3 structure as the ground state of $LuMnO_3$. Furthermore, it is quite difficult to determine the x coordinate from powder diffraction measurements so that for $YMnO_3$, which has been

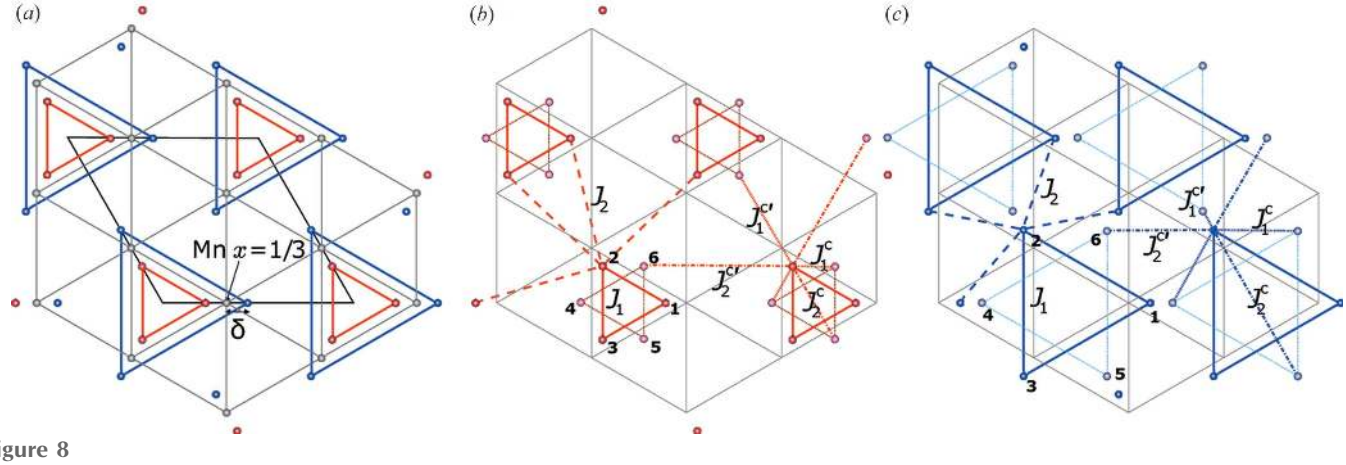

Figure 8
(*a*) Pattern of Mn trimerization with two different values of the Mn x position with Mn ions forming smaller trimers (red) or larger trimers (blue) on the *ab* plane. The different magnetic exchange interactions are shown for the case of (*b*) $x<\frac{1}{3}$ and (*c*) $x>\frac{1}{3}$.

well studied, values vary between $x = 0.3208$ and 0.336 at room temperature (Muñoz *et al.*, 2000; Park *et al.*, 2010). For other *h*-RMnO$_3$ compounds, in some cases both $x > \frac{1}{3}$ and $x < \frac{1}{3}$ have been reported for the same compounds, so it is difficult to establish systematic trends between the crystal and magnetic structures definitively. Nonetheless, the spin reorientation transition observed in HoMnO$_3$ presents a way to test this prediction: above T_{SR} where the structure is Γ_4, one would expect to observe $x < \frac{1}{3}$, whilst below T_{SR} the structure is Γ_3, implying $x > \frac{1}{3}$, so that at the transition one expects to see $x = \frac{1}{3}$. Neutron diffraction measurements by Fabrèges *et al.* (2009), reproduced in Fig. 9(*b*), appear to support this hypothesis, albeit with sizeable uncertainties.

Despite this, the effect of magnetic ordering on the crystal lattice is clear. Anomalies have been observed in the physical properties at T_N: in the elastic constants (Poirier *et al.*, 2007) and dielectric permittivity (Katsufuji *et al.*, 2001), as shown in Figs. 7(*c*) and (*d*). The lattice constants and unit-cell volume have also been observed to deviate from that expected from a Debye–Grüneisen model (Park *et al.*, 2010), as demonstrated in Fig. 7(*b*). However, the most striking illustration of this spin-lattice coupling is the astonishing observation by Lee *et al.* (2008) of the strong enhancement of the K_1 distortion below T_N in YMnO$_3$ (LuMnO$_3$), where the Mn x coordinate increases (decreases) significantly from $\frac{1}{3}$ below T_N, as reproduced in Fig. 9(*a*). This may be explained if the gain in the single-ion anisotropy (SIA) energy by further displacing the Mn ions is greater than the costs in elastic energy.

Another facet of the strong spin-lattice coupling is the observation that the magnetic domains in *h*-RMnO$_3$ are clamped to the ferroelectric domains (Fiebig *et al.*, 2002). There are three possible structural rotational directions of the MnO$_5$ polyhedra in the *ab* plane, denoted α, β and γ. The ferroelectric domains are then defined by the two possible directions of tilt of the apical oxygen ions, leading to the six possible structural-polarization domains $\alpha^{\pm}$, $\beta^{\pm}$ and $\gamma^{\pm}$, which form the characteristic vortex structure observed in microscopy measurements (Chae *et al.*, 2012, 2013). Each of these domains may be described by a phase angle Φ, which represents the angle to the displaced apical oxygen ions in that domain, and the sequence -120, -60, $\ldots +180^{\circ}$ corresponds to $\gamma^+, \beta^-, \alpha^+, \gamma^-, \beta^+, \alpha^-$. It is energetically favourable for this phase angle to only change by 60° between adjacent domains, which thus favours combined antiphase and ferroelectric domain walls, *e.g.* from α^+ to β^- or γ^-, but not to α^- (Artyukhin *et al.*, 2013; Kumagai & Spaldin, 2013). As each pair of antiphase domains $\alpha^{\pm}$, $\beta^{\pm}$ and $\gamma^{\pm}$ is related to a particular magnetic domain due to the preference of the moments to align along or perpendicular to the direction of the Mn displacement as the result of the trimerization distortion, this explains why the magnetic domains are locked to the ferroelectric ones (Artyukhin *et al.*, 2013). We note that purely magnetic domains, where the moments are rotated by 180° across the domain wall, can also exist within a single ferroelectric domain. In sum, the dependence of the magnetic moment on the unit-cell tripling distortions, which drives the ferroelectric order in *h*-RMnO$_3$, provides the mechanism for the magneto-electric coupling in these materials.

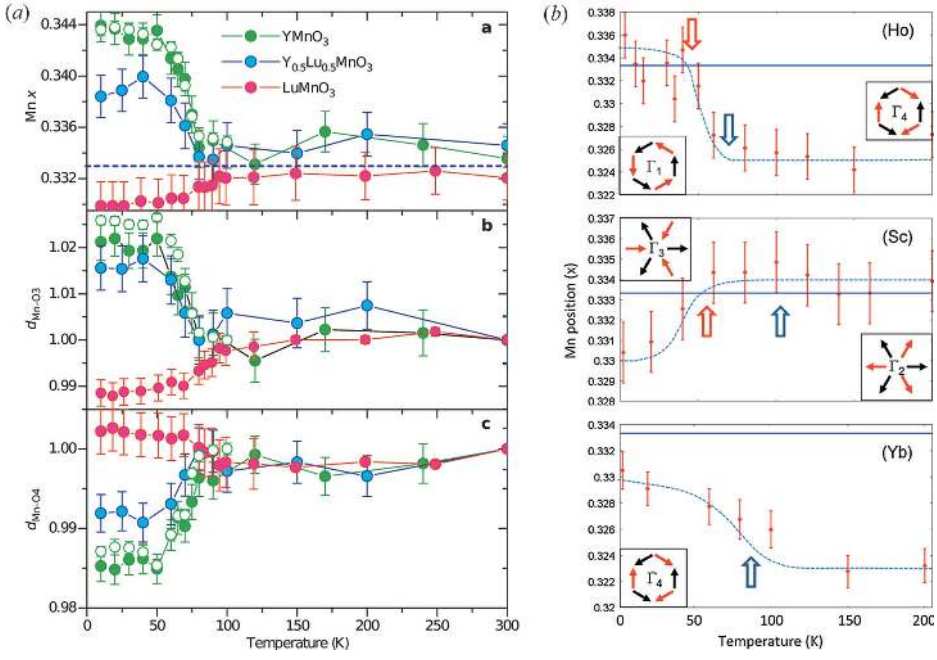

Figure 9
Temperature dependence of the Mn x position on (*a*) Y/LuMnO$_3$ and (*b*) Ho, Sc, YbMnO$_3$. Mn x position is one of the most important parameters in understanding the antiferromagnetic ordering and the spin reorientations of RMnO$_3$. These figures show the temperature dependence of the Mn atomic position for several RMnO$_3$, reprinted with permission from Lee *et al.* (2008) (Copyright © 2008, Nature) and Fabrèges *et al.* (2009) (Copyright © 2009, Americal Physical Society).

3. Excitations

As described in the previous sections, one can obtain great insight into the behaviour of the *h*-RMnO$_3$ compounds from their crystal and magnetic structure and how this changes with temperature or field. However, arguably the ultimate determination of the microscopic Hamiltonian of the system can only be obtained by studying the dynamics of the atoms (phonons) and magnetic moments (magnons). This will thus provide complementary information to the static behaviour of the structures and also the coupling between the spins and the lattice, the subject of the preceding sections. Furthermore, the magnetic excitations from the MnO layers, which form a frustrated two-dimensional triangular lattice, are themselves of fundamental interest. In this

Table 1
Summary of zone-center phonon modes calculated from the shell model and measured by Raman and IR spectroscopy.

Values are taken from: [1] Iliev *et al.* (1997), [2] Toulouse *et al.* (2014), [3] Zaghrioui *et al.* (2008), [4] Litvinchuk *et al.* (2004), [5] Basistyy *et al.* (2014) and [6] Vermette *et al.* (2010).

		$YMnO_3$				$HoMnO_3$					$LuMnO_3$	
Direction and sign of the largest displacement	Sym.	Shell (TO, LO) [1]		Raman 10 K [2]	IR 300 K [3]	Shell (TO, LO) [4]		Raman 300 K [4]		IR(TO) 10 K [5]	Raman 10 K [6]	IR(TO) 10 K [5]
$+z$(R1), $-z$(R2)	A_1	147	147	164	154	125	127	–	–	123.5	124	–
Rot. x, y(MnO_5)	A_1	204	216	211	–	195	234	–	–	223	228	–
$+z$(R1,R2), $-z$(Mn)	A_1	222	269	262	235	245	270	262	262	256	267	–
x(Mn), z(O3)	A_1	299	301	279	260	291	295	295	295	298	305	–
$+z$(O3), $-z$(O4), $+x, y$(O2), $-x, y$(O1)	A_1	388	398	–	304	404	428	411	–	–	–	–
$+z$(O4,O3), $-z$(Mn)	A_1	423	467	434	432	430	460	427	427	–	435	–
$+x, y$(O1,O2), $-x, y$(Mn)	A_1	492	496	467	486	468	474	463	463	486.1	475	–
$+z$(O1,O2), $-z$(Mn)	A_1	588	601		562	598	614	–	–	580.5	–	–
$+z$(O1), $-z$(O2)	A_1	662	662	685	–	673	673	685	685	–	692	–
$+x, y$(Mn,O3,O4), $-x, y$(R1,R2)	E_1	117	118	–	–	107	110	–	–	151.5	–	147.1
$+x, y$(R1), $-x, y$(R2)	E_1	147	149	–	162	143	143	–	–	–	–	155.5
$+x, y$(R2), $-x, y$(R1)	E_1	158	158	–	–	149	149	–	–	165.5	–	162.1
$+x, y$(O1,O2), $-x, y$(R1,R2)	E_1	212	231	–	207	231	231	–	–	–	–	182.4
x, y(Mn,O3), z(O1,O2)	E_1	233	245	–	249	247	253	–	–	245	–	270.5
$+x, y$(O1,O2), $-x, y$(O3)	E_1	250	337	–	299	262	336	–	–	266.5	–	273.5
$+x, y$(O1,O2,O3), $-x, y$(O4,Mn)	E_1	353	367	–	380	337	358	–	–	292.5	–	303.3
$+x, y$(O1), $-x, y$(O2)	E_1	390	403	–	400	359	397	354	308	–	313	–
$+x, y$(O1), $-x, y$(O2)	E_1	410	415	–	416	398	410	369	368	385	368	–
$+x, y$(O4,O3), $-x, y$(O2,O1,Mn)	E_1	459	477	–	–	471	491	419	–	–	415	–
$+x, y$(O4,O3,O1,O2), $-x, y$(Mn)	E_1	492	527	–	–	497	537	480	420	–	428	–
x, y(O4)	E_1	559	559	–	–	568	571	–	–	–	–	528
x, y(O3)	E_1	586	589	–	594	585	586	–	–	591	–	600
x, y(O3), $-x, y$(O4)	E_1	635	635	–	–	648	648	636	–	644	–	–
x, y(R1,R2,Mn)	E_2	71	85	–	64	–	–	–	–	–	–	–
$+x, y$(Mn,O3,O4), $-x, y$(R1,R2)	E_2	108	–	–	96	–	–	–	–	–	–	–
$+x, y$(R1), $-x, y$(R2)	E_2	136	142	–	137	136	–	–	–	–	–	–
$+x, y$(R2), $-x, y$(R1)	E_2	161	–	–	152	–	–	–	–	–	–	–
$+x, y$(O2,Mn), $-x, y$(O1,O3)	E_2	212	–	–	231	221	–	–	–	–	–	–
z(Mn,O2,O1)	E_2	241	235	–	254	–	–	–	–	–	–	–
z(Mn,O1,O2)	E_2	245	249	–	265	–	–	–	260	–	–	–
$+z$(O2), $-z$(O1), x, y(O4)	E_2	336	309	–	330	295	–	315	–	–	–	–
$+x, y$(O1,O2,O4,O3), $-x, y$(Mn)	E_2	382	376	–	339	–	–	–	345	–	–	–
$+x, y$(O1,O4), $-x, y$(O2,Mn)	E_2	407	418	–	402	–	–	–	–	–	–	–
$+x, y$(O4), $-x, y$(O1,Mn)	E_2	458	442	–	468	442	–	463	–	–	–	–
$+x, y$(O4,O3), $+x, y$(O1,O2)	E_2	515	–	–	523	–	–	–	–	–	–	–
x, y(O4)	E_2	557	–	–	557	–	–	–	–	–	–	–
x, y(O4,O3)	E_2	580	–	–	583	–	–	–	–	–	–	–
x, y(O3,O4)	E_2	638	637	–	649	–	–	–	–	–	–	–

section, we will review the optical and neutron spectroscopy studies on the excitation spectra of *h*-$RMnO_3$ with particular attention to its connection to the structural issue.

3.1. Phonons

Phonons are quantized portions of energies, describing lattice vibration waves. The properties of these waves are described in the reciprocal spaces. In the long wavelength limit, the possible vibrating modes are determined from the crystal symmetry while phonon energies are sensitive to the interaction strengths between the atoms. Therefore, long-wavelength optical phonons are sensitive to the changes in crystal symmetry and atom positions. The zone center phonon modes in *h*-$RMnO_3$ have been studied experimentally (using Raman, THz and IR spectroscopies), as well as theoretically (using shell model and first-principle calculations; Iliev *et al.*, 1997; Litvinchuk *et al.*, 2004; Fukumura *et al.*, 2007; Vermette *et al.*, 2008, 2010; Ghosh *et al.*, 2009; Liu *et al.*, 2012; Toulouse *et al.*, 2014; Goian *et al.*, 2010; Kadlec *et al.*, 2011; Souchkov *et al.*, 2003; Kovács *et al.*, 2012; Zaghrioui *et al.*, 2008; Basistyy *et al.*, 2014; Rushchanskii & Ležaić, 2012; Varignon *et al.*, 2012).

In the high-temperature paraelectric $P6_3/mmc$ phase, there are altogether 18 phonon modes, of which five are Raman active ($A_{1g} + E_{1g} + 3E_{2g}$) and six are IR active ($3A_{2u} + 3E_{1u}$). Fukumura *et al.* (2007) reported measurements of the Raman spectrum up to 1200 K and observed changes around 1000 K, which they attributed to a transition from $P6_3cm$ to $P6_3/mmc$. This is in contrast to the observed diffraction patterns, which showed that this transition is above 1200 K, as discussed in §2.1. Moreover, a more detailed study by Bouyanfif *et al.* (2015) showed clear evidence of another transition at 1200 K.

Thus, we think the four modes observed by Fukumura *et al.* (2007) should be interpreted within the polar $P6_3cm$ symmetry.

In the ferroelectric $P6_3cm$ phase, the unit cell is tripled, resulting in 60 phonon modes at the Γ point: among which 38 are Raman active ($9A_1 + 14E_1 + 15E_2$) and 23 are IR active ($9A_1 + 14E_1$). Early Raman and IR studies on $YMnO_3$ and $HoMnO_3$ identified many of the modes with the A_1, E_1 and E_2 symmetry and compared these with the shell model calculations (Iliev *et al.*, 1997; Litvinchuk *et al.*, 2004). In most cases, fewer phonon modes were experimentally observed than are allowed by symmetry, which makes it difficult to match them with the calculated modes. For example, only 8 (9) out of 14 possible E_1 (E_2) modes and 7 out of 9 possible A_1 modes have been observed for $YMnO_3$ even in the most extensive Raman and IR measurements (Toulouse *et al.*, 2014; Zaghrioui *et al.*, 2008). Although they have been assigned to the nearest energy modes in the shell model calculations, some ambiguities still remain in all practical likelihood.

A recent IR measurement on $LuMnO_3$, however, may shed light on this problem, finding 13 E_1 modes out of 14 (Basistyy *et al.*, 2014). Adopting the highest energy mode at 644 cm^{-1} found in Raman spectroscopy (Vermette *et al.*, 2010), the energies of all the possible E_1 modes were determined. Moreover, as the mass of Ho is similar to Lu, it is reasonable to assume that the phonon energies of $HoMnO_3$ are similar to that of $LuMnO_3$. Therefore, we can assign the phonon modes of $HoMnO_3$ to the nearest phonon modes in $LuMnO_3$, following the analysis used in Basistyy *et al.* (2014). Note that this mode assignment results in higher phonon energies compared with the shell model calculations, especially for the low-energy modes as shown in Table 1. Such discrepancies may possibly be due to oversimplifications in the shell model calculations. Indeed, first-principle electronic structure calculations of $YMnO_3$ tend to give higher phonon energies for the low-energy E_1 modes, when compared with those of the shell model calculations (Rushchanskii & Ležaić, 2012; Varignon *et al.*, 2012). Thus, further theoretical studies on the phonon spectra of $RMnO_3$ with heavy rare-earth elements are required for a more comprehensive understanding of their lattice dynamics.

3.2. Magnons

Like phonons, magnons are quantized spin waves in magnetically ordered crystals. They are completely described by their dispersion relation $\omega(\mathbf{q})$, where $\mathbf{q}$ is the wavevector. Measurements of this dispersion are sufficient to determine the underlying interactions that govern the spin dynamics, such as exchange interactions and single ion anisotropies.

3.2.1. High-energy spin dynamics: super-exchange interaction. The dominant magnetic interaction that determines the 120° spin structure is the nearest neighbor superexchange interaction in the triangular Mn—O layer. Several inelastic neutron scattering experiments have so far reported the magnon dispersion relations for various *h*-$RMnO_3$ compounds (Sato *et al.*, 2003; Vajk *et al.*, 2005; Chatterji *et al.*, 2007; Lewtas *et al.*, 2010; Fabrèges *et al.*, 2009; Oh *et al.*, 2013; Tian *et al.*, 2014; Chaix *et al.*, 2014). A simple spin Hamiltonian including only Heisenberg interactions in the Mn—O layer is given by

$$\mathcal{H} = J_1 \sum_{\text{intra}} \mathbf{S}_i \cdot \mathbf{S}_j + J_2 \sum_{\text{inter}} \mathbf{S}_i \cdot \mathbf{S}_j. \quad (1)$$

The two different exchange parameters J_1 and J_2 are due to the Mn trimerization as shown in Fig. 8. The magnon spectra can be calculated using Holstein–Primakoff operators (Holstein & Primakoff, 1940) (see also *Appendix A*).

The two different values of the exchange interaction are most apparent in the high-energy part of the magnon dispersion along the $[h, 1-2h, 0]$ direction, as shown in Fig. 10. If $J_1 \neq J_2$, the triple degeneracy of the magnons at the *K* point is lifted, resulting in one doubly degenerate mode at high energy and the other at lower energy. When $|J_2|>|J_1|$, the high-energy mode along the *M*—K direction is almost degenerate, while three different modes are evident for $|J_1|>|J_2|$. Inelastic neutron scattering studies have reported that a Hamiltonian with $J_1 \neq J_2$ is appropriate for $YMnO_3$ and $LuMnO_3$ (Sato *et al.*, 2003; Oh *et al.*, 2013), while a Hamiltonian with $J_1 = J_2$ describes well the measured excitations of $HoMnO_3$ (Vajk *et al.*, 2005). They are consistent with neutron powder diffraction results, which found that the Mn *x* coordinate deviates from $\frac{1}{3}$ for $YMnO_3$ and $LuMnO_3$ while it approaches the $\frac{1}{3}$ position for $HoMnO_3$ at low temperatures (Fabrèges *et al.*, 2009; Lee *et al.*, 2008; Park *et al.*, 2010). However, theoretical calculations (Solovyev *et al.*, 2012) using the coordinates reported by Lee *et al.* (2008) yielded $J_1/J_2 \simeq 0.8$ (~ 1.1) for $YMnO_3$ ($LuMnO_3$), which is quite different from $J_1/J_2 \simeq 1.5$ (~ 6) determined from the inelastic neutron scattering experiments. Therefore, it appears that to explain the large J_1/J_2 ratio determined from the experiments on $LuMnO_3$, a much larger shift of the Mn *x* position is necessary. However, this is unlikely to be the case since the reported changes in the atom positions are already

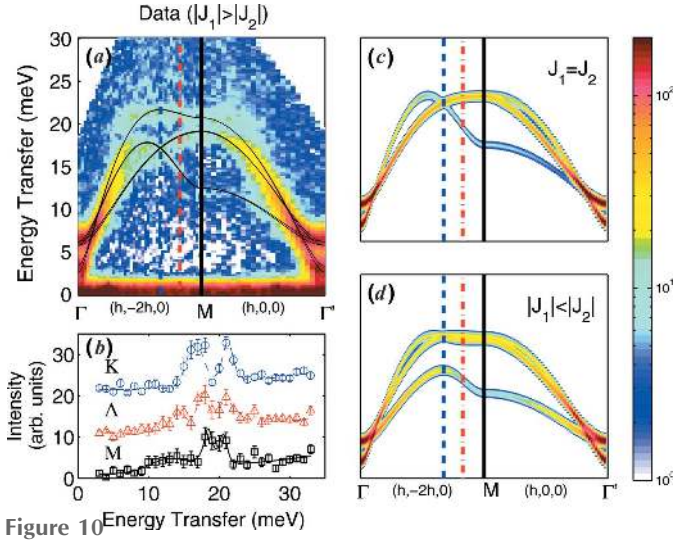

Figure 10 Magnon spectra for different J_1 and J_2 values. (*a*) Experimental magnon dispersion for $LuMnO_3$. (*b*) Constant *q* cut at the high symmetry points. (*c*), (*d*) Simulation results with $J_1 = J_2$ and $J_1 < J_2$ models. Reprinted with permission from Oh *et al.* (2013) (Copyright © 2013, Americal Physical Society).

quite large (Lee *et al.*, 2008). Thus, the standard interpretation of the magnon spectra reviewed above may need to be revised, and further effects such as magnon–phonon coupling or magnon–magnon interactions should be taken into account. These will be discussed in §3.3 and §3.4.

3.2.2. Low-energy spin dynamics: inter-layer coupling and single ion anisotropy. Although the Hamiltonian above describes the high-energy magnon spectra quite well, the inter-layer super exchange interaction and the single ion anisotropy are necessary to explain the various possible magnetic structures, as discussed in §2.3. The inter-layer interaction determines the angle between the spins in alternating triangular layers, while the single ion anisotropies fix the directions of the spins. The final full spin Hamiltonian thus includes four different exchange parameters (J_1, J_2, J_1^c and J_2^c), an easy-plane anisotropy (D_1) and easy-axis anisotropy (D_2) (see *Appendix A*). It turns out that the inter-layer interactions and easy-axis anisotropy are over two orders of magnitude smaller than the dominant in-plane exchange interactions, showed by a small dispersion along the c^* direction and a small spin anisotropy gap (Sato *et al.*, 2003; Fabrèges *et al.*, 2009; Oh *et al.*, 2013).

However, it is difficult to uniquely determine these parameters from unpolarized inelastic neutron scattering experiments. For example, the change of the sign in J_1^c–J_2^c modifies the magnon intensity along the $[h\,0\,l]$ direction whilst a 90° rotation of the easy-axis anisotropy has exactly the same effects. Therefore, the parameter sets giving the Γ_1 (Γ_2) spin configurations and those giving Γ_3 (Γ_4) result in the same magnon spectra (see Fig. 11). Thus, unpolarized inelastic neutron scattering, like unpolarized neutron diffraction, cannot distinguish between the two constituents of a homometric pair. Nonetheless, the structures determined from the combination of SHG and diffraction measurements can be

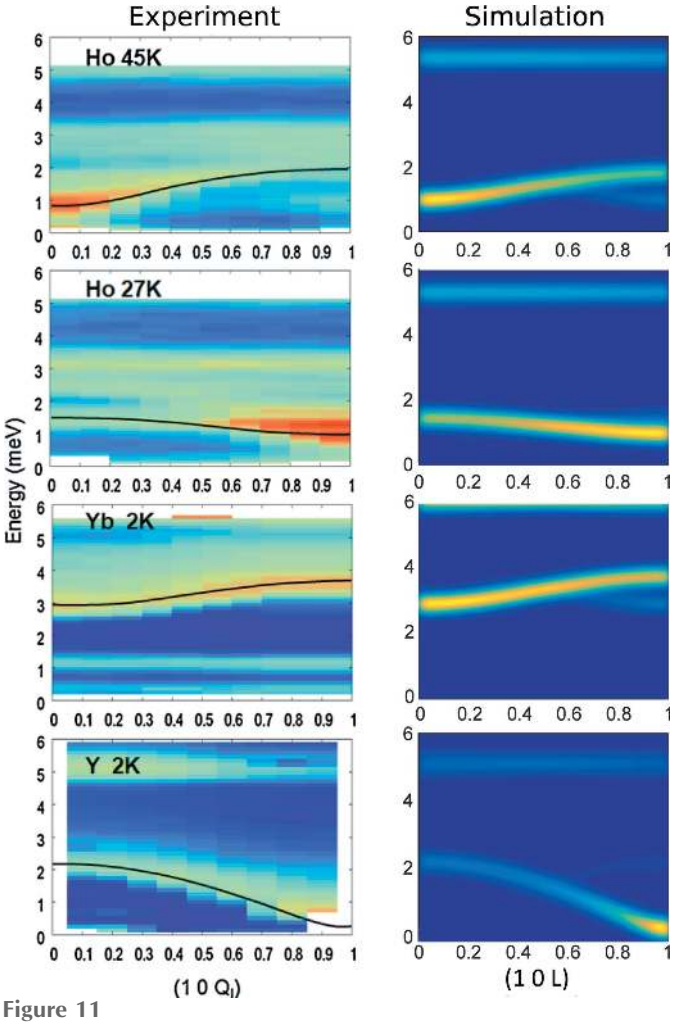

Figure 11
(*a*) Experimental magnon spectra along the 10*l* direction for different compounds: (*b*) our calculated results that are reproduced by using the following set of parameters: $J_1^c - J_2^c = 0.006$, $D_1 = 0.3$, $D_2 = -0.005$ meV for $HoMnO_3$ at 45 K: $J_1^c - J_2^c = 0.003$, $D_1 = 0.3$, $D_2 = -0.005$ meV for $HoMnO_3$ at 27 K: $J_1^c - J_2^c = 0.015$, $D_1 = 0.35$, $D_2 = -0.045$ meV for $YbMnO_3$: $J_1^c - J_2^c = 0.014$, $D_1 = 0.28$, $D_2 = -0.0007$ meV for $YMnO_3$. The experimental results are reprinted with permission from Fabrèges *et al.* (2009) (Copyright © 2009, American Physical Society).

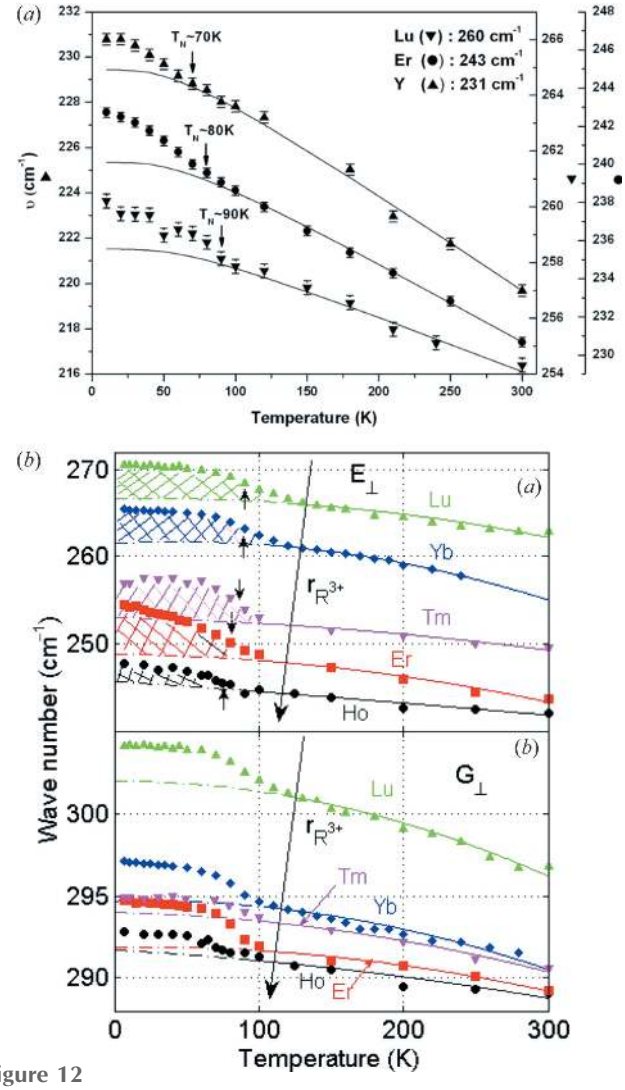

Figure 12
(*a*) E_2 phonon modes and (*b*) E_1 phonon modes that show visible changes below T_N for different compounds. Reprinted with permission from Vermette *et al.* (2010) (Copyright © IOP Publishing) and Basistyy *et al.* (2014) (Copyright © 2014, American Physical Society).

used to obtain the exact parameter sets from the analysis of inelastic neutron scattering data.

3.3. Spin-phonon coupling

The mechanism underlying the spin-lattice coupling discussed in §2.3 can be investigated further by measuring the changes in the phonon modes as the antiferromagnetic order develops or by observing the hybridization of magnon and phonon modes. Several IR and Raman measurements have shown that many phonon modes shift in energy below T_N (Vermette *et al.*, 2010; Fukumura *et al.*, 2007, 2009; Ghosh *et al.*, 2009; Vermette *et al.*, 2008; Litvinchuk *et al.*, 2004; Basistyy *et al.*, 2014). For example, Vermette *et al.* (2010) found that the E_2 mode near 250 cm^{-1}, reproduced in Fig. 12(*a*), shows a kink at T_N and hardens below the temperature. Further IR studies by Basistyy *et al.* (2014) on R = Ho, Er, Tm, Yb and Lu as reproduced in Fig. 12(*b*) gave similar behaviour for the phonon energies, and reflect the change in vibrations of the manganese and oxygen ions within the triangular plane due to the structure distortion that occurs with the onset of the Néel order.

A related aspect is the hybridization of magnon and acoustic phonon modes, which have been observed by inelastic neutron scattering. Petit *et al.* (2007) found that a gap appears in the transverse acoustic phonon mode of $YMnO_3$ below T_N at around $q_0 \simeq 0.185$, as shown in Fig. 13. The observed phonon displacement parallel to the c^* axis indicates that the spin couples to the out-of-plane atomic motions. Further polarized inelastic neutron scattering studies by Pailhès *et al.* (2009) showed that the upper split mode has both nuclear and magnetic character, indicating that it is indeed a hybrid mode. However, only anti-crossing behaviour was observed at high $|q|$, whilst at low $|q|$ the magnon spectrum showed no gap. This is different from the well studied magnon–phonon hybridization in materials with strong single ion magnetostriction, which shows a gap opening in both the phonon (high $|q|$) and magnon (low $|q|$) dispersions. Furthermore, the reciprocal lattice point at $q_{cross} \simeq 0.3$, where the magnon and phonon modes cross, does not coincide with the position q_0 of the gap. This then implies that the magnon–phonon coupling may also have some q dependence in order to explain the experimental data.

There are three main spin-lattice coupling mechanisms that can exist in *h*-RMnO$_3$: single ion magnetostriction (Van Vleck, 1940), spin current (Katsura *et al.*, 2005) and exchange-striction (Dharmawardana & Mavroyannis, 1970). The hardening, below T_N, of the zone center phonon modes that modulates Mn—O—Mn bond lengths and angles has been attributed to the exchange striction model (Litvinchuk *et al.*, 2004; Vermette *et al.*, 2010; Basistyy *et al.*, 2014), whilst the spin rotation transitions, as discussed in §2.3, results from the equilibrium single ion magnetostriction. However, there is yet no consensus on the origin of the observed magnon–phonon hybridization. For example, it has been attributed by Petit *et al.* (2007) to the dynamic single ion magnetostriction, in which the motions of the atoms modulate the crystal field of the Mn ions that determines the single-ion anisotropy. Pailhès *et al.* (2009), on the other hand, favours the spin-current mechanism, where it is the Dzyaloshinsky–Moriya (DM) interactions that are modulated. We also note that the single ion anisotropy in *h*-RMnO$_3$, $D \simeq 0.3$ meV (Sato *et al.*, 2003), is of the same order of magnitude as FeF_2, where strong magnon–phonon hybridization have been observed (Hutchings *et al.*, 1970; Lovesey, 1972). For comparison, the component of the DM interaction that gives rise to the spin canting is an order of magnitude smaller than the single ion anisotropy D (Solovyev *et al.*, 2012). On the other hand, there has been no study of the exchange-striction effects on the magnon–phonon

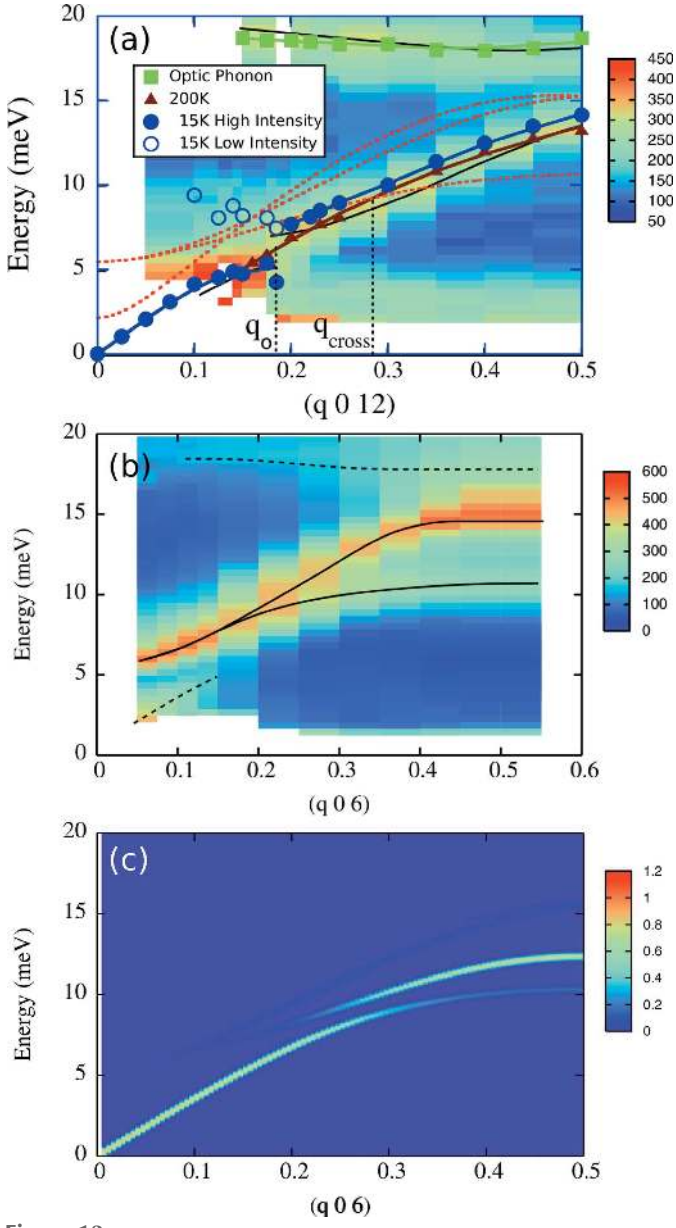

Figure 13
Experimentally measured and theoretically calculated phonon and magnon modes: (*a*) a gap in the acoustic phonon mode observed in $YMnO_3$ below T_N at high $|q|$; (*b*) no gap in the magnon dispersion at lower $|q|$; (*c*) the simulation result. Reprinted with permission from Petit *et al.* (2007) (Copyright © 2007, American Physical Society).

coupling in *h*-RMnO$_3$. This is probably because the exchange-striction effects only allow an anharmonic coupling between magnons and phonons in collinear spin systems, and thus has been theoretically neglected. However, a linear coupling is allowed in noncollinear magnets (Hasegawa *et al.*, 2010; Kim & Han, 2007) and, moreover, the exchange-striction scenario is believed to be the mechanism underlying the electromagnon observed in orthorhombic RMnO$_3$ (Valdés Aguilar *et al.*, 2009). Thus, the next question to be answered is how much each of these three different mechanisms contribute to the spin-phonon coupling in *h*-RMnO$_3$.

3.4. Spontaneous magnon decays

The magnon spectra have been interpreted within the linear spin wave theory in §3.2. In the linear spin wave theory, terms higher than quadratic in $a_i^\dagger$ (creation operator) and a_i (annihilation operator) are neglected. In this case, a magnon is stable with an infinite lifetime. The next higher-order terms allowed in collinear magnets are quartic terms giving interactions between magnons, analogous to the Coulomb interactions in electron systems. Although this results in finite magnon lifetimes at non-zero temperatures, the magnon is a stable quasiparticle at zero temperature (Harris *et al.*, 1971; Dyson, 1956; Bayrakci *et al.*, 2013). In magnets with noncollinear spin structures, however, the next order terms are the cubic terms, which gives an interaction between one and two magnon states that is otherwise forbidden in collinear magnets. This allows the decay of a magnon into two magnon states that results in finite magnon lifetimes even at the zero temperature (Chernyshev & Zhitomirsky, 2006, 2009). This phenomenon is called 'spontaneous magnon decays' and was recently reviewed by Zhitomirsky & Chernyshev (2013).

One of the simplest systems with a noncollinear spin structure is the two-dimensional triangular lattice Heisenberg antiferromagnet (TLHA). Therefore, its spectra have been most studied theoretically amongst noncollinear magnets (Chernyshev & Zhitomirsky, 2006; Starykh *et al.*, 2006; Zheng *et al.*, 2006*a*,*b*; Chernyshev & Zhitomirsky, 2009; Mourigal *et al.*, 2013). However, the experimental verification of these theoretical predictions is challenging mainly due to the scarcity of (nearly) ideal two-dimensional TLHA found in nature. For example, dimensional reduction in Cs_2CuCl_4 (Coldea *et al.*, 2001; Kohno *et al.*, 2007) and strong next-nearest neighbor interactions in α-$CaCr_2O_4$ (Toth *et al.*, 2012) make their spin excitation spectra quite different from that predicted for the ideal two-dimensional TLHA. *h*-RMnO$_3$, in contrast, provides a rare opportunity, as their magnon spectra have proven to be very similar to those of the ideal case (Chatterji *et al.*, 2007; Vajk *et al.*, 2005).

A recent inelastic neutron scattering study found the clearest evidence of spontaneous magnon decays in LuMnO$_3$ (Oh *et al.*, 2013). For example, the line width of the top-most magnon mode is significantly broadened compared with the experimental resolution near $q = (0.5, 0.5, 0)$, as shown in Fig. 14(*a*). Furthermore, the energy and the q position at this point coincides with the regions of large, two-magnon density states, as shown in Fig. 14(*b*). Note that a magnon can only decay into two-magnon states with the same momentum and energy since the momentum and energy should be preserved during the decay process (Zhitomirsky & Chernyshev, 2013). Therefore, these two-magnon states overlapping with the single-magnon dispersion results in many decay channels. Thus, the observed broadening can be interpreted as the result of a reduced magnon lifetime due to the enhanced decay channels.

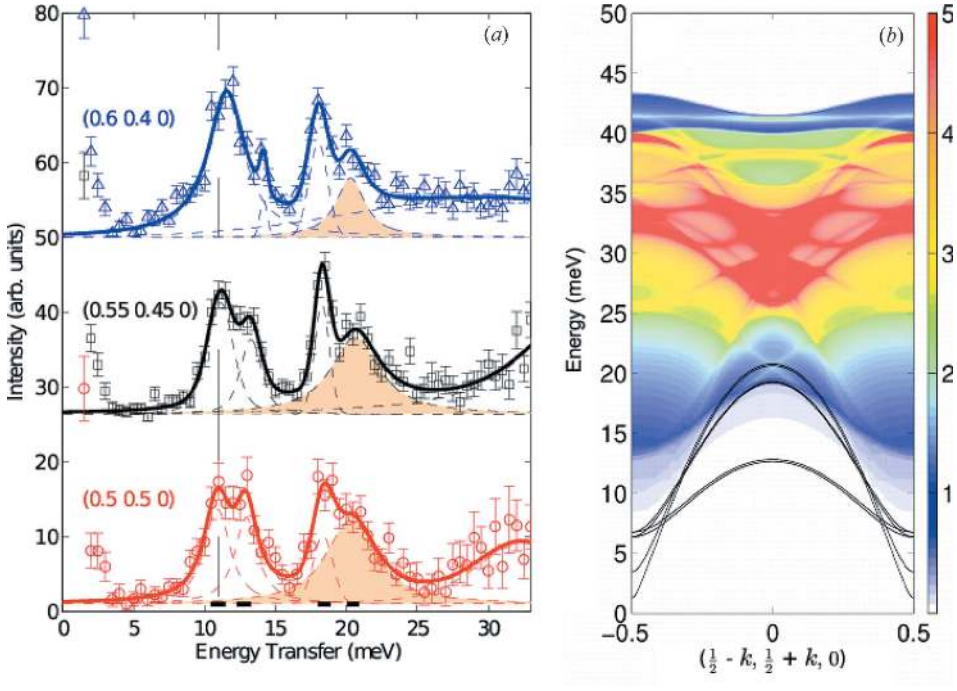

Figure 14
(*a*) Linewidth broadening of the top-most mode of the spin waves measured at $q = (0.5, 0.5, 0)$ for LuMnO$_3$ and (*b*) the calculated two-magnon density of states. Reprinted with permission from Oh *et al.* (2013) (Copyright © 2013, American Physical Society).

4. Summary and outlook

Ever since Curie (1894) conjectured on 'the symmetry in physical phenomena, symmetry of an electric field and a magnetic field', it has long been a dream for material scientists to search for this rather unusual class of materials exhibiting the coexistence of magnetism and ferroelectricity in a single compound. Thanks to the extensive volume of works carried out worldwide over the past decade or so, we have now expanded the list of such materials far beyond the

few that were studied in Russia in the 1960s (Astrov, 1961; Astrov *et al.*, 1969; Smolenskii *et al.*, 1968). This experimental renaissance of multiferroic physics seems to give a long overdue justification to the earlier pioneering theoretical works, mainly in the names of two great scientists: Dzyaloshinskii (1958) and Moriya (1960).

Of such a long list of multiferroic materials, the hexagonal manganites $R\mathrm{MnO_3}$ and $\mathrm{BiFeO_3}$ stand out most for various reasons. In the case of $\mathrm{BiFeO_3}$, most of the studies were driven by the fact that it is the only compound showing multiferroic behavior at room temperature: all the other multiferroic materials known to date exhibit this unusual ground state only at low temperature (Park *et al.*, 2014). On the other hand, hexagonal $R\mathrm{MnO_3}$ has been extensively investigated using various methods, both experimental and theoretical as it has a two-dimensional triangular lattice. As has been reviewed in this article, it offers a rare yet fascinating playground where we can explore the combined physics of multiferroic and frustration effects (Diep, 2005; Gardner *et al.*, 2010; Ramirez, 1994), in addition to testing our understanding of two-dimensional triangular antiferromagnetism (Collins & Petrenko, 1997).

First of all, when the antiferromagnetic ground state kicks in at around 80–100 K with the so-called 120° coplanar magnetic structure, lowered by a factor of 6 compared with its Curie–Weiss temperature, it gives rise to an extremely large and unusual in-plane deformation of Mn—O layers (Lee *et al.*, 2008; Poirier *et al.*, 2007; Souchkov *et al.*, 2003; Litvinchuk *et al.*, 2004). When this in-plane deformation occurs, there are subsequent atomic displacements of similar magnitude along the *c*-axis. So not surprisingly, this gigantic spin-lattice coupling induces an extra 0.5 $\mu\mathrm{C\ cm^{-2}}$ of electric polarization, which then provides the necessary coupling among the three otherwise independent degrees of freedom: lattice, spin and electric polarization (Lee *et al.*, 2005). At the same time, this unusual spin-lattice coupling is also seen to play a crucial role in suppressing thermal conductivity (Sharma *et al.*, 2004).

As if this amazing display of a spin-lattice coupling in the structural studies is not enough, yet more surprises come from studying spin dynamics. Its almost ideal triangular lattice and its readily available high-quality single crystals make it a perfect system to explore the spin dynamics of a Heisenberg spin in a triangular lattice. It turns out that the 120° coplanar, noncollinear magnetic structure is actually crucial in hosting the hitherto largely ignored effects of magnon–magnon coupling. For example, our detailed studies of spin waves in $\mathrm{LuMnO_3}$ unearthed, for the first time, three key experimental pieces of evidence for magnon–magnon coupling: a roton-like minimum, flat mode and magnon decay (Oh *et al.*, 2013). All three of these effects were previously predicted for a triangular magnetic system with noncollinear magnetic ground states (Zheng *et al.*, 2006*a*; Chernyshev & Zhitomirsky, 2006; Starykh *et al.*, 2006). Furthermore, we found more recently that there are nontrivial coupling effects of magnon–phonon on the spin dynamics (Oh *et al.*, 2016). All these works of spin dynamics further illustrate how intimately connected the structural aspect of the $R\mathrm{MnO_3}$ physics is to their spin dynamics.

In this review, we have examined the structure and spin dynamics of this interesting class of materials. Furthermore, we have also looked at an interesting possibility by using *h*-$R\mathrm{MnO_3}$ of how we can further deepen our understanding of two-dimensional triangular antiferromagnetism (Collins & Petrenko, 1997), in particular magnon–magnon (Zhitomirsky & Chernyshev, 2013) or magnon–phonon coupling (Wang & Vishwanath, 2008; Valdés Aguilar *et al.*, 2009).

APPENDIX *A*
Calculation of magnon dispersion relation and dynamical structure factor

A standard way of calculating magnon spectra for the Γ_4 spin structure is given in this section. The other spin configurations can be handled in a similar manner. The full spin Hamiltonian is given by

$$\begin{aligned}\mathcal{H} = {} & J_1 \sum_{\text{intra}} \mathbf{S}_i \cdot \mathbf{S}_j + J_2 \sum_{\text{inter}} \mathbf{S}_i \cdot \mathbf{S}_j \\ & + J_1^c \sum_{\text{outintra}} \mathbf{S}_i \cdot \mathbf{S}_j + J_2^c \sum_{\text{outinter}} \mathbf{S}_i \cdot \mathbf{S}_j \\ & + D_1 \sum_i (\mathbf{S}_i^z)^2 + D_2 \sum_i (\mathbf{S}_i \cdot \mathbf{n}_i)^2, \end{aligned} \tag{2}$$

where $\mathbf{n}_i$ is a unit vector parallel to the spin direction at the ith site in the Γ_4 configuration (see Figs. 5 and 8). The spin operators at six sublattices can be expressed using Holstein–Primakoff operators as shown by the following equations

$$\begin{aligned} S_i^x &= \frac{\sqrt{2S}}{2i}(a_i - a_i^\dagger) \\ S_i^y &= S - a_i a_i^\dagger \\ S_i^z &= \frac{\sqrt{2S}}{2}(a_i + a_i^\dagger) \end{aligned} \tag{3}$$

$$\begin{aligned} S_j^x &= -\frac{\sqrt{3}}{2}(S - a_j a_j^\dagger) - \frac{1}{2}\frac{\sqrt{2S}}{2i}(a_j - a_j^\dagger) \\ S_j^y &= -\frac{1}{2}(S - a_j a_j^\dagger) + \frac{\sqrt{3}}{2}\frac{\sqrt{2S}}{2i}(a_j - a_j^\dagger) \\ S_j^z &= \frac{\sqrt{2S}}{2}(a_j + a_j^\dagger) \end{aligned} \tag{4}$$

$$\begin{aligned} S_k^x &= \frac{\sqrt{3}}{2}(S - a_k a_k^\dagger) - \frac{1}{2}\frac{\sqrt{2S}}{2i}(a_k - a_k^\dagger) \\ S_k^y &= -\frac{1}{2}(S - a_k a_k^\dagger) - \frac{\sqrt{3}}{2}\frac{\sqrt{2S}}{2i}(a_k - a_k^\dagger) \\ S_k^z &= \frac{\sqrt{2S}}{2}(a_k + a_k^\dagger), \end{aligned} \tag{5}$$

where $i = 1, 4$, $j = 2, 5$ and $k = 3, 6$. After substituting equations (3)–(5) into equation (2), leaving out terms not higher than the quadratic of $a^\dagger$ (creation operator) and a (annihila-

tion operator), and performing Fourier transformation, the Hamiltonian can be rewritten in the following matrix form

$$\mathcal{H} = -6\Delta S(S+1)N + \sum_k \mathbf{X}^\dagger \begin{pmatrix} \mathbf{U} & \mathbf{V} \\ \mathbf{V} & \mathbf{U} \end{pmatrix} \mathbf{X}, \qquad (6)$$

where

$$\mathbf{U} = \begin{pmatrix} \mathbf{P} + \Delta \mathbf{I}_3 & \mathbf{Q} + \mathbf{R} \\ \mathbf{Q}^* + \mathbf{R}^* & \mathbf{P}^* + \Delta \mathbf{I}_3 \end{pmatrix},$$
$$\mathbf{V} = \begin{pmatrix} 3\mathbf{P} + D_1 \mathbf{I}_3 & 3\mathbf{Q} \\ 3\mathbf{Q}^* & 3\mathbf{P}^* + D_1 \mathbf{I}_3 \end{pmatrix}, \qquad (7)$$

$$\mathbf{X} = \begin{pmatrix} a_{1,k} \\ \vdots \\ a_{6,k} \\ a_{1,-k} \\ \vdots \\ a_{6,-k} \end{pmatrix}, \quad \begin{aligned} \mathbf{P} &= \begin{pmatrix} 0 & A^* & C \\ A & 0 & B^* \\ C^* & B & 0 \end{pmatrix}, \\ \mathbf{Q} &= \begin{pmatrix} 0 & A' & A' \\ A' & 0 & A' \\ A' & A' & 0 \end{pmatrix}, \\ \mathbf{R} &= \begin{pmatrix} B' & 0 & 0 \\ 0 & B' & 0 \\ 0 & 0 & B' \end{pmatrix}, \end{aligned}$$

and

$$\begin{aligned} A &= \frac{1}{8}\left[J_1 + J_2\left(e^{-ik\cdot b} + e^{-ik\cdot(a+b)}\right)\right], \\ B &= \frac{1}{8}\left[J_1 + J_2\left(e^{-ik\cdot a} + e^{ik\cdot b}\right)\right], \\ C &= \frac{1}{8}\left[J_1 + J_2\left(e^{ik\cdot a} + e^{ik\cdot(a+b)}\right)\right], \\ \Delta &= \frac{1}{2}(J_1 + 2J_2 + 2J_1^c - 2J_2^c + D_1 - 2D_2), \\ A' &= \frac{J_1^c}{8}\left(1 + e^{-ik\cdot c}\right), \\ B' &= \frac{J_2^c}{2}\left(1 + e^{-ik\cdot c}\right). \end{aligned} \qquad (9)$$

Here, a, b and c denote the lattice unit vectors and $\mathbf{I}_3$ is a 3×3 identity matrix. The numerical diagonalization of the matrix form above results in six magnon modes. The obtained eigenvalues and eigenvectors are used to obtain the magnon dispersion and dynamical structure factor. For more details of the calculation, see White *et al.* (1965) and Petit (2011).

Acknowledgements

This review is the direct result of our extensive works on hexagonal $R\mathrm{MnO_3}$ over the years. Therefore, we should acknowledge all the past and present members of the group who have contributed to our research on this material directly or indirectly. Moreover, it goes without saying that we have benefited enormously from our extensive network of collaborations. In particular we should mention a few names who made significant contributions to our understanding of the topics summarized in this review: S.-W. Cheong, Seongsu Lee, Junghwan Park, T. Kamiyama, Y. Noda, A. Pirogov, D. P. Kozlenko, T. G. Perring & W. J. L. Buyers. This work was supported by the research programme of Institute for Basic Science (IBS-R009-G1).

References

Abrahams, S. C. (2001). *Acta Cryst.* B**57**, 485–490.
Alonso, J. A., Martínez-Lope, M. J., Casais, M. T. & Fernández-Díaz, M. T. (2000). *Inorg. Chem.* **39**, 917–923.
Artyukhin, S., Delaney, K. T., Spaldin, N. A. & Mostovoy, M. (2013). *Nat. Mater.* **13**, 42–49.
Astrov, D. (1961). *Sov. Phys. JETP*, **13**, 729–733.
Astrov, D., Al'Shin, B., Zorin, R. & Drobyshev, L. (1969). *Sov. Phys. JETP*, **28**, 1123.
Basistyy, R., Stanislavchuk, T. N., Sirenko, A. A., Litvinchuk, A. P., Kotelyanskii, M., Carr, G. L., Lee, N., Wang, X. & Cheong, S.-W. (2014). *Phys. Rev. B*, **90**, 024307.
Bayrakci, S. P., Tennant, D. A., Leininger, P., Keller, T., Gibson, M. C. R., Wilson, S. D., Birgeneau, R. J. & Keimer, B. (2013). *Phys. Rev. Lett.* **111**, 017204.
Bergum, K., Okamoto, H., Fjellvåg, H., Grande, T., Einarsrud, M.-A. & Selbach, S. M. (2011). *Dalton Trans.* **40**, 7583–7589.
Bouyanfif, H., Salah, A. M., Zaghrioui, M. & El Marssi, M. (2015). *Phys. Rev. B*, **91**, 224104.
Brown, P. J. & Chatterji, T. (2006). *J. Phys. Condens. Matter*, **18**, 10085–10096.
Chae, S. C., Horibe, Y., Jeong, D. Y., Lee, N., Iida, K., Tanimura, M. & Cheong, S.-W. (2013). *Phys. Rev. Lett.* **110**, 167601.
Chae, S. C., Lee, N., Horibe, Y., Tanimura, M., Mori, S., Gao, B., Carr, S. & Cheong, S.-W. (2012). *Phys. Rev. Lett.* **108**, 167603.
Chaix, L., de Brion, S., Petit, S., Ballou, R., Regnault, L. P., Ollivier, J., Brubach, J. B., Roy, P., Debray, J., Lejay, P., Cano, A., Ressouche, E. & Simonet, V. (2014). *Phys. Rev. Lett.* **112**, 137201.
Chatterji, T., Ghosh, S., Singh, A., Regnault, L. P. & Rheinstädter, M. (2007). *Phys. Rev. B*, **76**, 144406.
Chatterji, T., Hansen, T., Kimber, S. A. J. & Bhattacharya, D. (2014). *Solid State Commun.* **180**, 46–51.
Chernyshev, A. L. & Zhitomirsky, M. E. (2006). *Phys. Rev. Lett.* **97**, 207202.
Chernyshev, A. L. & Zhitomirsky, M. E. (2009). *Phys. Rev. B*, **79**, 144416.
Cho, D. Y., Kim, J. Y., Park, B. G., Rho, K. J., Park, J. H., Noh, H. J., Kim, B. J., Oh, S. J., Park, H. M., Ahn, J. S., Ishibashi, H., Cheong, S. W., Lee, J. H., Murugavel, P., Noh, T. W., Tanaka, A. & Jo, T. (2007). *Phys. Rev. Lett.* **98**, 217601.
Choi, T., Hong, S., Abrahamson, J. T., Han, J., Song, C., Nair, N., Baik, S. & Strano, M. S. (2010). *Nat. Mater.* **9**, 423–429.
Choi, Y. J., Lee, N., Sharma, P. A., Kim, S. B., Vajk, O. P., Lynn, J. W., Oh, Y. S. & Cheong, S. W. (2013). *Phys. Rev. Lett.* **110**, 157202.
Coeuré, P., Guinet, P., Peuzin, J. C., Buisson, G. & Bertaut, E. F. (1966). *Proc. Int. Meet. Ferroelectr.* **1**, 332–340.
Coldea, R., Tennant, D. A., Tsvelik, A. M. & Tylczynski, Z. (2001). *Phys. Rev. Lett.* **86**, 1335–1338.
Collins, M. F. & Petrenko, O. A. (1997). *Can. J. Phys.* **75**, 605–655.
Curie, P. (1894). *J. Phys. Theor. Appl.* **3**, 393–415.
Curnoe, S. H. & Munawar, I. (2006). *Phys. B Condens. Matter*, **378–380**, 554–555.
Das, H., Wysocki, A. L., Geng, Y., Wu, W. & Fennie, C. J. (2014). *Nat. Commun.* **5**, 2998.
Degenhardt, C., Fiebig, M., Fröhlich, D., Lottermoser, T. & Pisarev, R. V. (2001). *Appl. Phys. B*, **73**, 139–144.
dela Cruz, C., Yen, F., Lorenz, B., Wang, Y. Q., Sun, Y. Y., Gospodinov, M. M. & Chu, C. W. (2005). *Phys. Rev. B*, **71**, 060407.
Dharmawardana, M. W. C. & Mavroyannis, C. (1970). *Phys. Rev. B*, **1**, 1166–1179.
Diep, H. T. (2005). Editor. *Frustrated Spin Systems*. Singapore: World Scientific.
Dyson, F. J. (1956). *Phys. Rev.* **102**, 1217–1230.
Dzyaloshinskii, I. (1958). *J. Phys. Chem. Solids*, **4**, 241–255.

Fabrèges, X., Mirebeau, I., Bonville, P., Petit, S., Lebras-Jasmin, G., Forget, A., André, G. & Pailhès, S. (2008). *Phys. Rev. B*, **78**, 214422.
Fabrèges, X., Petit, S., Mirebeau, I., Pailhès, S., Pinsard, L., Forget, A., Fernandez-Diaz, M. T. & Porcher, F. (2009). *Phys. Rev. Lett.* **103**, 067204.
Fan, C., Zhao, Z. Y., Song, J. D., Wu, J. C., Zhang, F. B. & Sun, X. F. (2014). *J. Cryst. Growth*, **388**, 54–60.
Fennie, C. J. & Rabe, K. M. (2005). *Phys. Rev. B*, **72**, 100103.
Fiebig, M., Fröhlich, D., Kohn, K., Leute, S., Lottermoser, T., Pavlov, V. V. & Pisarev, R. V. (2000). *Phys. Rev. Lett.* **84**, 5620–5623.
Fiebig, M., Lottermoser, T., Fröhlich, D., Goltsev, A. V. & Pisarev, R. V. (2002). *Nature*, **419**, 818–820.
Fiebig, M., Lottermoser, T. & Pisarev, R. V. (2003). *J. Appl. Phys.* **93**, 8194–8196.
Fiebig, M., Pavlov, V. V. & Pisarev, R. V. (2005). *J. Opt. Soc. Am. B*, **22**, 96.
Fukumura, H., Hasuike, N., Harima, H., Kisoda, K., Fukae, K., Yoshimura, T. & Fujimura, N. (2009). *J. Phys. Condens. Matter*, **21**, 064218.
Fukumura, H., Matsui, S., Harima, H., Kisoda, K., Takahashi, T., Yoshimura, T. & Fujimura, N. (2007). *J. Phys. Condens. Matter*, **19**, 365239.
Gardner, J. S., Gingras, M. J. P. & Greedan, J. E. (2010). *Rev. Mod. Phys.* **82**, 53–107.
Ghosh, A., Sahu, J. R., Bhat, S. V. & Rao, C. N. R. (2009). *Solid State Sci.* **11**, 1639–1642.
Gibbs, A., Knight, K. & Lightfoot, P. (2011). *Phys. Rev. B*, **83**, 094111.
Goian, V., Kamba, S., Kadlec, C., Nuzhnyy, D., Kužel, P., Agostinho Moreira, J., Almeida, A. & Tavares, P. B. (2010). *Phase Transitions*, **83**, 931–941.
Harikrishnan, S., Rösler, S., Naveen Kumar, C. M., Bhat, H. L., Rösler, U. K., Wirth, S., Steglich, F. & Elizabeth, S. (2009). *J. Phys. Condens. Matter*, **21**, 096002.
Harris, A. B., Kumar, D., Halperin, B. I. & Hohenberg, P. C. (1971). *Phys. Rev. B*, **3**, 961–1024.
Hasegawa, T., Miyahara, S. & Furukawa, N. (2010). *J. Phys. Conf. Ser.* **200**, 012053.
Holstein, T. & Primakoff, H. (1940). *Phys. Rev.* **58**, 1098–1113.
Hur, N., Jeong, I. K., Hundley, M. F., Kim, S. B. & Cheong, S. W. (2009). *Phys. Rev. B*, **79**, 134120.
Hutchings, M. T., Rainford, B. D. & Guggenheim, H. J. (1970). *J. Phys. C Solid State Phys.* **3**, 307–322.
Iliev, M. N., Lee, H.-G., Popov, V. N., Abrashev, M. V., Hamed, A., Meng, R. L. & Chu, C. W. (1997). *Phys. Rev. B*, **56**, 2488–2494.
Ismailzade, I. G. & Kizhaev, S. A. (1965*a*). *Fiz. Tverd. Tela*, **7**, 298.
Ismailzade, I. G. & Kizhaev, S. A. (1965*b*). *Sov. Phys. Solid State*, **7**, 236.
Iwata, N. & Kohn, K. (1998). *Ferroelectrics*, **219**, 161–168.
Kadlec, C., Goian, V., Rushchanskii, K. Z., Kužel, P., Ležaić, M., Kohn, K., Pisarev, R. V. & Kamba, S. (2011). *Phys. Rev. B*, **84**, 174120.
Katsufuji, T., Masaki, M., Machida, A., Moritomo, M., Kato, K., Nishibori, E., Takata, M., Sakata, M., Ohoyama, K., Kitazawa, K. & Takagi, H. (2002). *Phys. Rev. B*, **66**, 134434.
Katsufuji, T., Mori, S., Masaki, M., Moritomo, Y., Yamamoto, N. & Takagi, H. (2001). *Phys. Rev. B*, **64**, 104419.
Katsura, H., Nagaosa, N. & Balatsky, A. V. (2005). *Phys. Rev. Lett.* **95**, 057205.
Kim, J., Cho, K. C., Koo, Y. M., Hong, K. P. & Shin, N. (2009). *Appl. Phys. Lett.* **95**, 132901.
Kim, J. H. & Han, J. H. (2007). *Phys. Rev. B*, **76**, 054431.
Kimura, T., Goto, T., Shintani, H., Ishizaka, K., Arima, T. & Tokura, Y. (2003). *Nature*, **426**, 55–58.
Kohno, M., Starykh, O. A. & Balents, L. (2007). *Nat. Phys.* **3**, 790–795.
Kovács, L., Lengyel, K. & Gospodinov, M. (2012). *Ferroelectrics*, **428**, 82–86.
Kumagai, Y. & Spaldin, N. A. (2013). *Nat. Commun.* **4**, 1540.
Lee, S., Pirogov, A., Han, J. H., Park, J.-G., Hoshikawa, A. & Kamiyama, T. (2005). *Phys. Rev. B*, **71**, 180413.
Lee, S., Pirogov, A., Kang, M., Jang, K.-H., Yonemura, M., Kamiyama, T., Cheong, S.-W., Gozzo, F., Shin, N., Kimura, H., Noda, Y. & Park, J.-G. (2008). *Nature*, **451**, 805–808.
Lewtas, H. J., Boothroyd, A. T., Rotter, M., Prabhakaran, D., Müller, H., Le, M. D., Roessli, B., Gavilano, J. & Bourges, P. (2010). *Phys. Rev. B*, **82**, 184420.
Litvinchuk, A. P., Iliev, M. N., Popov, V. N. & Gospodinov, M. M. (2004). *J. Phys. Condens. Matter*, **16**, 809–819.
Liu, J., Toulouse, C., Rovillain, P., Cazayous, M., Gallais, Y., Measson, M. A., Lee, N., Cheong, S. W. & Sacuto, A. (2012). *Phys. Rev. B*, **86**, 184410.
Lonkai, T., Tomuta, D. G., Amann, U., Ihringer, J., Hendrikx, R. W. A., Többens, D. M. & Mydosh, J. A. (2004). *Phys. Rev. B*, **69**, 134108.
Lorenz, B. (2013). *ISRN Condens. Matter Phys.* **2013**, 497073.
Lorenz, B., Yen, F., Gospodinov, M. M. & Chu, C. W. (2005). *Phys. Rev. B*, **71**, 014438.
Lovesey, S. W. (1972). *J. Phys. C Solid State Phys.* **5**, 2769–2784.
Mochizuki, M., Furukawa, N. & Nagaosa, N. (2011). *Phys. Rev. B*, **84**, 144409.
Moriya, T. (1960). *Phys. Rev.* **120**, 91–98.
Mourigal, M., Fuhrman, W. T., Chernyshev, A. L. & Zhitomirsky, M. E. (2013). *Phys. Rev. B*, **88**, 094407.
Muñoz, A., Alonso, J. A., Martínez-Lope, M. J., Casáis, M. T., Martínez, J. L. & Fernández-Díaz, M. T. (2000). *Phys. Rev. B*, **62**, 9498–9510.
Nénert, G., Pollet, M., Marinel, S., Blake, G. R., Meetsma, A. & Palstra, T. T. M. (2007). *J. Phys. Condens. Matter*, **19**, 466212.
Nénert, G., Ren, Y., Stokes, H. T. & Palstra, T. T. M. (2005). arXiv: cond-Mater/0504546.
Oh, J. *et al.* (2016). In preparation.
Oh, J., Le, M. D., Jeong, J., Lee, J. H., Woo, H., Song, W. Y., Perring, T. G., Buyers, W. J. L., Cheong, S. W. & Park, J. G. (2013). *Phys. Rev. Lett.* **111**, 257202.
Pailhès, S., Fabrèges, X., Régnault, L. P., Pinsard-Godart, L., Mirebeau, I., Moussa, F., Hennion, M. & Petit, S. (2009). *Phys. Rev. B*, **79**, 134409.
Park, J., Kong, U., Choi, S. I., Park, J.-G., Lee, C. & Jo, W. (2002). *Appl. Phys. Mater. Sci. Process.* **74**, s802–s804.
Park, J.-G., Le, M. D., Jeong, J. & Lee, S. (2014). *J. Phys. Condens. Matter*, **26**, 433202.
Park, J., Lee, S., Kang, M., Jang, K. H., Lee, C., Streltsov, S. V., Mazurenko, V. V., Valentyuk, M. V., Medvedeva, J. E., Kamiyama, T. & Park, J. G. (2010). *Phys. Rev. B*, **82**, 054428.
Petit, S. (2011). *Collection SFN*, **12**, 105–121.
Petit, S., Moussa, F., Hennion, M., Pailhès, S., Pinsard-Gaudart, L. & Ivanov, A. (2007). *Phys. Rev. Lett.* **99**, 266604.
Poirier, M., Laliberté, F., Pinsard-Gaudart, L. & Revcolevschi, A. (2007). *Phys. Rev. B*, **76**, 174426.
Ramirez, A. P. (1994). *Annu. Rev. Mater. Sci.* **24**, 453–480.
Rushchanskii, K. Z. & Ležaić, M. (2012). *Ferroelectrics*, **426**, 90–96.
Sato, T. J., Lee, S. H., Katsufuji, T., Masaki, M., Park, S., Copley, J. R. D. & Takagi, H. (2003). *Phys. Rev. B*, **68**, 014432.
Sekhar, M. C., Lee, S., Choi, G., Lee, C. & Park, J. G. (2005). *Phys. Rev. B*, **72**, 014402.
Sharma, P. A., Ahn, J. S., Hur, N., Park, S., Kim, S. B., Lee, S., Park, J. G., Guha, S. & Cheong, S. W. (2004). *Phys. Rev. Lett.* **93**, 177202.
Smolenskii, G., Bokov, V., Isupov, V., Krainik, N. & Nedlin, G. (1968). *Helv. Phys. Acta*, **41**, 1187.
Solovyev, I. V., Valentyuk, M. V. & Mazurenko, V. V. (2012). *Phys. Rev. B*, **86**, 054407.
Souchkov, A. B., Simpson, J. R., Quijada, M., Ishibashi, H., Hur, N., Ahn, J. S., Cheong, S. W., Millis, A. J. & Drew, H. D. (2003). *Phys. Rev. Lett.* **91**, 027203.
Starykh, O. A., Chubukov, A. V. & Abanov, A. G. (2006). *Phys. Rev. B*, **74**, 180403.

Sugie, H., Iwata, N. & Kohn, K. (2002). *J. Phys. Soc. Jpn*, **71**, 1558–1564.
Tian, W., Tan, G., Liu, L., Zhang, J., Winn, B., Hong, T., Fernandez-Baca, J. A., Zhang, C. & Dai, P. (2014). *Phys. Rev. B*, **89**, 144417.
Tong, P., Louca, D., Lee, N. & Cheong, S. W. (2012). *Phys. Rev. B*, **86**, 094419.
Toth, S., Lake, B., Hradil, K., Guidi, T., Rule, K. C., Stone, M. B. & Islam, A. T. M. N. (2012). *Phys. Rev. Lett.* **109**, 127203.
Toulouse, C., Liu, J., Gallais, Y., Measson, M.-A., Sacuto, A., Cazayous, M., Chaix, L., Simonet, V., de Brion, S., Pinsard-Godart, L., Willaert, F., Brubach, J. B., Roy, P. & Petit, S. (2014). *Phys. Rev. B*, **89**, 094415.
Tyson, T. A., Wu, T., Chen, H. Y., Bai, J., Ahn, K. H., Pandya, K. I., Kim, S. B. & Cheong, S. W. (2011). *J. Appl. Phys.* **110**, 084116.
Vajk, O. P., Kenzelmann, M., Lynn, J. W., Kim, S. B. & Cheong, S. W. (2005). *Phys. Rev. Lett.* **94**, 087601.
Valdés Aguilar, R., Mostovoy, M., Sushkov, A. B., Zhang, C. L., Choi, Y. J., Cheong, S.-W. & Drew, H. D. (2009). *Phys. Rev. Lett.* **102**, 047203.
Van Aken, B. B. & Palstra, T. T. M. (2004). *Phys. Rev. B*, **69**, 134113.
Van Aken, B. B., Palstra, T. T. M., Filippetti, A. & Spaldin, N. A. (2004). *Nat. Mater.* **3**, 164–170.
Van Vleck, J. H. (1940). *Phys. Rev.* **57**, 426–447.
Varignon, J., Petit, S. & Lepetit, M.-B. (2012). arXiv: 1203.1752.
Vermette, J., Jandl, S. & Gospodinov, M. M. (2008). *J. Phys. Condens. Matter*, **20**, 425219.
Vermette, J., Jandl, S., Mukhin, A. A., Ivanov, V. Y., Balbashov, A., Gospodinov, M. M. & Pinsard-Gaudart, L. (2010). *J. Phys. Condens. Matter*, **22**, 356002.
Wang, F. & Vishwanath, A. (2008). *Phys. Rev. Lett.* **100**, 077201.
White, R. M., Sparks, M. & Ortenburger, I. (1965). *Phys. Rev. A*, **139**, 450–454.
Yen, F., dela Cruz, C., Lorenz, B., Galstyan, E., Sun, Y. Y., Gospodinov, M. & Chu, C. W. (2007). *J. Mater. Res.* **22**, 2163–2173.
Zaghrioui, M., Ta Phuoc, V., Souza, R. A. & Gervais, M. (2008). *Phys. Rev. B*, **78**, 184305.
Zheng, W., Fjaerestad, J. O., Singh, R. R. P., McKenzie, R. H. & Coldea, R. (2006*a*). *Phys. Rev. Lett.* **96**, 057201.
Zheng, W., Fjaerestad, J. O., Singh, R. R. P., McKenzie, R. H. & Coldea, R. (2006*b*). *Phys. Rev. B*, **74**, 224420.
Zhitomirsky, M. E. & Chernyshev, A. L. (2013). *Rev. Mod. Phys.* **85**, 219–242.
Zhou, J. S., Goodenough, J. B., Gallardo-Amores, J. M., Morán, E., Alario-Franco, M. & Caudillo, R. (2006). *Phys. Rev. B*, **74**, 014422.